LITHOS 518-519 (2025) 108317

Contents lists available at ScienceDirect

LITHOS

journal homepage: www.elsevier.com/locate/lithos

Carbonatitic metasomatism in ultramafic rocks at the Blue Hill, Namibia

Felix Reinhard [a,*], Benjamin F. Walter [a], R. Johannes Giebel [b,c], Armin Zeh [d], Michael A.W. Marks [a], Gregor Markl [a]

[a] Eberhard Karls University Tübingen, Schnarrenbergstraße 94–96, 72076 Tübingen, Germany
[b] Technical University of Berlin, Ernst-Reuter-Platz 1, 10587 Berlin, Germany
[c] University of the Free State, 250 Nelson-Mandela-Drive, Bloemfontein 9300, South Africa
[d] Karlsruher Institut für Technologie, Adenauerring 20b, 76131 Karlsruhe, Germany

ARTICLE INFO

Keywords:
Damtjernite
Fluids
Fenitization
Phlogopite chemistry
Age dating
Gross Brukkaros

ABSTRACT

Carbonatite metasomatism at crustal pressures can significantly modify igneous and sedimentary rocks and understanding these processes is critical for interpreting mantle-derived magmas and their associated carbonate-bearing fluids. The Blue Hill complex in Namibia, located within the carbonatitic Gross Brukkaros volcanic field, represents an ideal natural laboratory to study the interaction between ultramafic lamprophyres (damtjernites) and carbonatitic fluids. In this setting, the damtjernites occur in direct spatial association with numerous carbonatite dykes, enabling detailed investigation of alteration processes. Evidence from olivine, spinel and whole-rock chemistry supports a mantle-derived UML parental melt that experienced post-emplacement CO_2 degassing, contributing to monticellite formation and possibly the adjacent fenitization of the country rock. Three distinct alteration types are identified: textures A (serpentine-magnetite-phlogopite-chlorite) and B (pectolite-–apatite–hydrogarnet–calcite), which occur concentrically within the main complex, whereas C (phlogopite-serpentine-apatite-hydrogarnet-calcite) forms crosscutting veins. This study aims to explore to what extent the alteration of the damtjernite reflects carbonatitic activity within the Gibeon province. Texture A records mainly deuteric (late-magmatic) alteration with minor meteoric input, while texture C shows a clear carbonatitic signature with Ba-Al-rich phlogopite, Mg-calcite and abundant apatite. Texture B remains more complex and might represent either a separate CO_2-rich fluid, possibly related to texture C, or the evolved residue of the fluid responsible for texture A. Geochronological data is in accordance with a multi-stage history of magmatism and fluid interaction, with emplacement of the Blue Hill at 84 ± 4 Ma and later resetting at 60 ± 14 Ma. Notably, the first reported age for the nearby Gross Brukkaros carbonatite (66 ± 8 Ma) appears to be younger than the Blue Hill emplacement. These constrains provide one of the few documented examples of carbonatitic liquids modifying pre-existing ultramafic rocks, expanding our understanding of metasomatism in carbonatite-bearing provinces.

1. Introduction

Ultramafic lamprophyres (UML) are a diverse group of potassic alkaline igneous rocks, generally associated with lithospheric extension, rifting and continental break-up (Rock, 1986; Sudholz et al., 2023; Tappe et al., 2005). They typically exhibit a porphyritic texture with olivine and phlogopite macrocrysts, and can be melilite-, nepheline-, K-feldspar-, or garnet-bearing (Tappe et al., 2005).

UML-forming melts are commonly sourced from a phlogopite- and carbonate-bearing mantle that has been metasomatized by fluids potentially enriched by subducted sediments (Tappe et al., 2006; Veter et al., 2017). The relationships between UMLs and carbonatites that often occur associated with each other, are not fully understood (Krüger et al., 2013; Secher et al., 2009; Doroshkevich et al., 2022; Tappe et al., 2006). Carbonatite-forming melts may be mantle-derived, represent fractionation products or result from exsolved liquids originating from carbonate-bearing silicate melts sourced from the upper lithospheric mantle (Yaxley et al., 2022). Crustal assimilation introduces diverse silicate minerals into carbonatites. Fenitization represents alkali metasomatism of host rocks by magmatic-hydrothermal fluids (Elliott et al., 2018; Le Bas, 2008; Walter et al., 2021). Alternatively, carbonatite magma may directly react with silicate host rocks, forming so-called

* Corresponding author.
E-mail address: felix.reinhard@gmail.com (F. Reinhard).

https://doi.org/10.1016/j.lithos.2025.108317
Received 15 April 2025; Received in revised form 31 October 2025; Accepted 1 November 2025
Available online 7 November 2025

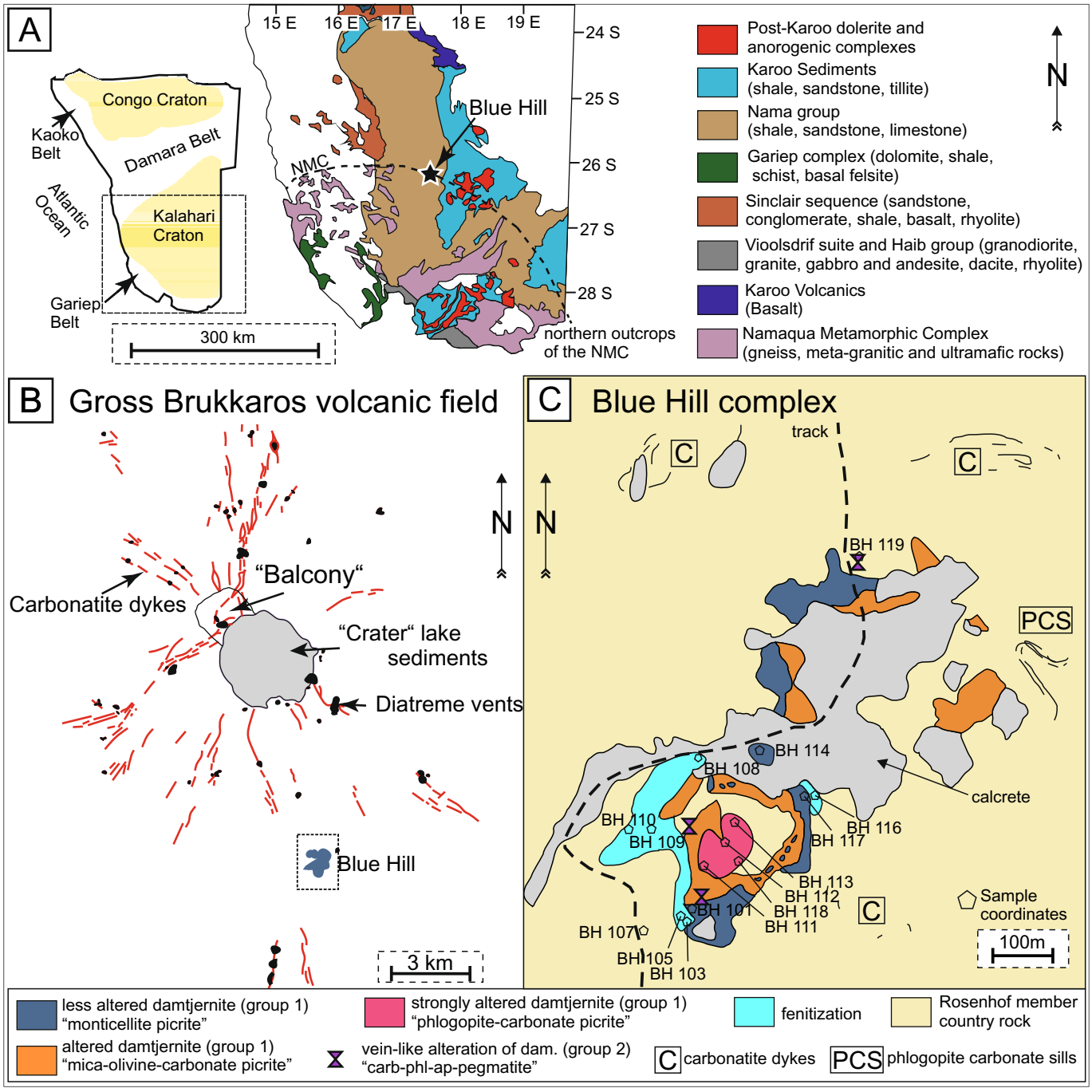

Fig. 1. A) Location of the Blue Hill in Namibia: geological map of Namibia (Walter et al., 2023 and references therein). Black star marks the location of the Blue Hill complex, situated on northern outcrops of the Namaqua Metamorphic Complex. B) Gross Brukkaros volcanic field: overview of radial carbonatite dykes and diatremes around the Gross Brukkaros (adapted from Walter et al., 2023; Lorenz et al., 2000). C) Map of the Blue Hill complex (modified after Kurszlaukis et al., 1999). Rock terms from this study are supplemented by older proposed names for comparison (in quotation marks). (For interpretation of the references to colour in this figure legend, the reader is referred to the web version of this article.)

antiskarns (sensu Anenburg and Mavrogenes, 2018). Unlike fenites, antiskarns involve exchange of Ca, Mg, Al, Si and Fe, although Si is the key factor, and develop within the carbonatite or at its margins (Anenburg and Mavrogenes, 2018). A more recent concept is the formation of associated ultramafic rocks in carbonatite complexes. These rocks were presumed to be of igneous origin, but recent studies (e.g. Anenburg and Walters, 2024; Vasyukova and Williams-Jones, 2022) suggest that they may instead form through carbonatitic metasomatism. Previously, the focus of carbonatitic metasomatism has been on mantle processes, but even at crustal pressures carbonatites appear to undergo a variety of interactions with silicate host rocks that remain to be fully explored. Carbonatitic metasomatism has often been described based on reactions between crustal felsic rocks (e.g. granites; Su et al., 2023) and carbonatitic liquids, but ultramafic rocks being metasomatically overprinted by carbonatites has only been rarely investigated in detail (Chmyz et al., 2022, 2025). This is the topic of the present paper.

2. Geological setting

The Blue Hill complex (25°56′S, 17°47′E) lies at the northern front of

Table 1
Sample list including methods that have been applied on sample.

Sample	Rock type	Samples group	Methods applied
BH117	Least altered damtjernite	Group 1	Whole rock, Micro-XRF, EPMA, U—Pb dating
BH-L-012/5	Least altered damtjernite	Group 1	Whole rock, EPMA, U—Pb dating
BH-L-004	Least altered damtjernite	Group 1	EPMA
BH101	Least altered damtjernite	Group 1	EPMA
BH-L-003	Altered damtjernite	Group 1	EPMA
BH-L-005	Altered damtjernite	Group 1	EPMA
BH-L-009/1	Altered damtjernite	Group 1	Whole rock, EPMA
BH113	Strongly altered damtjernite	Group 1	Whole rock, Micro-XRF, EPMA
BH118	Strongly altered damtjernite	Group 1	Micro-XRF, EPMA
BH115	Vein-like alteration of damtjernite	Group 2	Micro-XRF, EPMA
BH119	Vein-like alteration of damtjernite	Group 2	Whole rock, EPMA, Raman
BH107	Quartz-rich shale	Country rock	Whole rock
BH105	Fenite	Country rock	Whole rock, Micro-XRF
BH108	Fenite	Country rock	Whole rock, Micro-XRF
BH102A	Fenite	Country rock	Micro-XRF
BH103	Fenite	Country rock	Micro-XRF
BH109A	Fenite	Country rock	Micro-XRF
BH-L-002	Fenite	Country rock	Micro-XRF

the Pan-African granulite facies Namaqua Metamorphic Complex (Fig. 1A), part of the southern and western margins of the Kalahari Craton (Bial et al., 2015; Diener et al., 2017). It intruded into sediments of the Nama Basin and is hosted by flat-lying Rosenhof Member shales with interbedded quartzite layers of the Haribes Member (Fish River Subgroup, Nama Group; Kurszlaukis et al., 1999). The Nama Basin, a peripheral foreland basin of the Damara Belt, covers ~125,000 km^2 of Southwest Africa with sandstones, shales, and limestones unconformably overlying the Kalahari Craton basement (Blanco et al., 2011; Germs et al., 1986; Stanistreet et al., 1991). Regionally, the Blue Hill is part of the Gibeon Kimberlite-Carbonatite Province, which contains over 70 non-diamondiferous kimberlite dykes and diatremes across a 100 × 80 km area (Davies et al., 2001). Kimberlite dykes contain olivine and phlogopite macrocrysts in a fine-grained matrix of olivine, perovskite, spinel and monticellite with variable amounts of phlogopite, calcite, apatite and serpentine (Spriggs, 1988). Approximately 6.5 km north of the Blue Hill, the ring-shaped Gross Brukkaros mountain (7 km basal diameter, 600 m high) towers the landscape, marking the center of the Gross Brukkaros volcanic field (Fig. 1B; Stachel et al., 1994). This area includes over 100 radial carbonatitic dykes and 74 diatremes, with dykes up to 2 km length and diameters up to 200 m (Lorenz et al., 2000; Lorenz and Kurszlaukis, 1997). Stachel et al. (1994) proposed a three-stage genetic model: (1) laccolith-shaped intrusion bulging up the country rock, (2) erosion flattening the structure, and (3) caldera-like subsidence following magma depletion. Fluids partially silicified dome sediments, promoting heterogeneous erosion. While Gross Brukkaros remained undated, an Rb—Sr whole-rock–phlogopite isochron age of 71.5 ± 0.4 Ma has been reported for the Gibeon kimberlites (Davies et al., 2001). The Blue Hill complex was dated using Rb—Sr on phlogopite to 75.1 ± 0.6 Ma by Kurszlaukis (1994).

The Blue Hill is a laccolith-type intrusion, several hundred meters long, up to 45 m high and widely covered by calcrete and baked shales (Fig. 1C; Janse, 1971; Kurszlaukis et al., 1999). Janse (1971) identified a single magmatic lithology (monticellite peridotite) modified by alteration and genetically linked it to Gross Brukkaros via separation of volatile-rich and poor phases of a common kimberlitic parental melt. Spriggs (1988) refuted this, suggesting instead (1) an asthenospheric source in the dolomite stability field (80–110 km), shallower than Gibeon kimberlites, and (2) higher degrees of partial melting and oxygen fugacity than typical for kimberlite magmas. Kurszlaukis et al. (1999) distinguished three picritic intrusions (monticellite picrite, mica-olivine-carbonate picrite and phlogopite-carbonate picrite) along with an in-situ differentiated carbonate–phlogopite–apatite pegmatite (Fig. 1C). Based on differences in MgO/CaO ratios, olivine fractionation, and SiO_2 content compared to Gibeon kimberlites, they concluded that the parental melt was not kimberlitic but likely derived from a shallower mantle source in the dolomite peridotite stability field (100–110 km).

3. Methods

3.1. Petrographical analyses

Thin sections of the investigated samples were analyzed using transmitted light microscopy and a TESCAN VEGA scanning electron microscope (Karlsruhe Institute of Technology - KIT) in backscattered electron mode at 15 kV, equipped with an energy-dispersive X-ray spectrometer. Micro-XRF (M4 Tornado, Bruker) mapping (Technische Universität Berlin) was performed to visualize elemental distribution at thin-section scale, using a 50 kV acceleration voltage, 600 μA beam current, 30 μm point spacing, 20 μm beam diameter and 60 ms dwell time per spot.

3.2. Mineral analyses

Analyses of olivine, mica, perovskite, carbonate and garnet were performed using a JEOL JXA 8230 electron probe microanalyzer (EPMA) in wavelength-dispersive mode at the University of Tübingen. A focused beam was used, with counting times of 16 s for major and 30 s for minor and trace elements; background times were half those of peak measurements. Instrument settings (acceleration voltage, probe current, and beam diameter) were adjusted based on mineral sensitivity (see Supplementary Data A1). Calibration employed both synthetic and natural standards (Astimex CRMs). Peak overlap corrections were applied for Cr—V, Er—Fe, V—Ti, Cl—Nd, Gd—Ce, Pr—La, Ba—Ti, and Gd—La. All analyses used internal φ(ρz) raw data correction (Armstrong, 1991). Additional mineral-specific parameters are provided in Supplementary Data (A2–A7).

3.3. Raman micro-spectroscopy

Raman micro-spectroscopy was conducted on garnet from one sample using a confocal Raman micro-spectrometer (Renishaw InVia) at the University of Tübingen, equipped with a 532 nm green laser, 1800 grooves·mm^{-1} grating and a Peltier-cooled CCD detector. Laser power was initially set to 1 % and later adjusted to 5 %, with three accumulations per acquisition across the 100–4000 cm^{-1} spectral range.

3.4. Whole rock analyses

Major elements were determined by wavelength dispersive X-ray fluorescence spectroscopy with a Bruker AXS S4 Explorer at KIT. Samples were powdered with an oscillating disk mill and agate grinding set. Loss on ignition (LOI) was determined by heating powders at 950 °C for 3 h. Fused beads were prepared from a 1:10 mixture of sample and Li-tetraborate/Li-metaborate (66.5:33.5; Spectroflux 110, AlfaAeser) and melted at 1000–1100 °C. A Rh X-ray tube (50 keV, 1 kW), proportional flow (Ar–CH_4 gas) and scintillation counters and XS-55, LIF2000, and

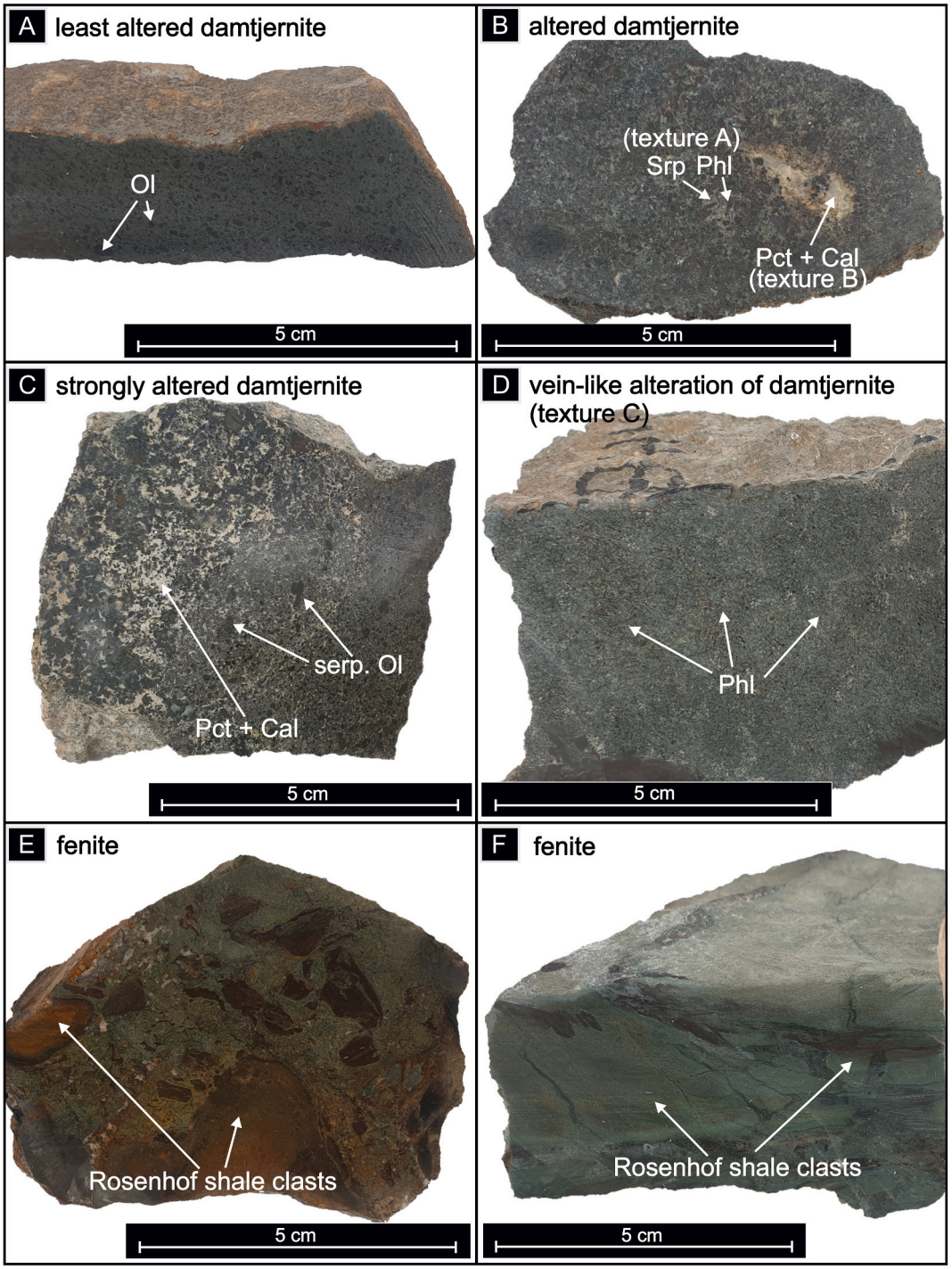

Fig. 2. Representative rock samples of the Blue Hill. Pictures A-C display the rocks with the highest voluminal abundance at the Blue Hill (group 1), altered by visible serpentine and phlogopite (texture A) and pectolite-calcite (texture B). Picture D portrays a rock variety with abundant macrocrystic phlogopite, only visible in small vein-like outcrops at the Blue Hill (texture C). Pictures E and F depict typical breccias of country rock associated with the Blue Hill complex. Mineral abbreviations: Cal – calcite, Ol – olivine, Pct – pectolite, Phl – phlogopite, Srp – serpentine. (For interpretation of the references to colour in this figure legend, the reader is referred to the web version of this article.)

PET crystals were used. Calibration utilized certified rock standards, while reference materials JDo-1, MEG-1 and Sy-2 confirmed measurement quality (accuracy >90 % for relevant elements).

Total C and S contents were measured with a carbon-sulfur analyzer (CS 2000 Eltra) at KIT. Powders mixed with Fe and W additives were combusted at 2000 °C in an induction furnace, converting C and S to CO_2 and SO_2. After dust and H_2O removal, infrared spectroscopy quantified the gases. Two certified standards – a steel (92400–3050) and a ductile iron (92400–3100) reference from Eltra - ensured accuracy (>93 %).

Trace elements were analyzed via ICP-MS (iCap RQ, Thermo Fisher) at KIT. Powdered samples (100 mg) were digested in 40 % HF (suprapur), 65 % $HClO_4$ (normatom) and 65 % HNO_3 (subboiled) and heated in closed Teflon vessels at 120 °C for 16 h. The dried residues were redissolved in 65 % HNO_3 and evaporated three times before final dilution in 50 mL ultrapure water. Measurement quality was assessed with certified reference materials SY-2 VF2 (Syenite), MEG-1, and JDo-1

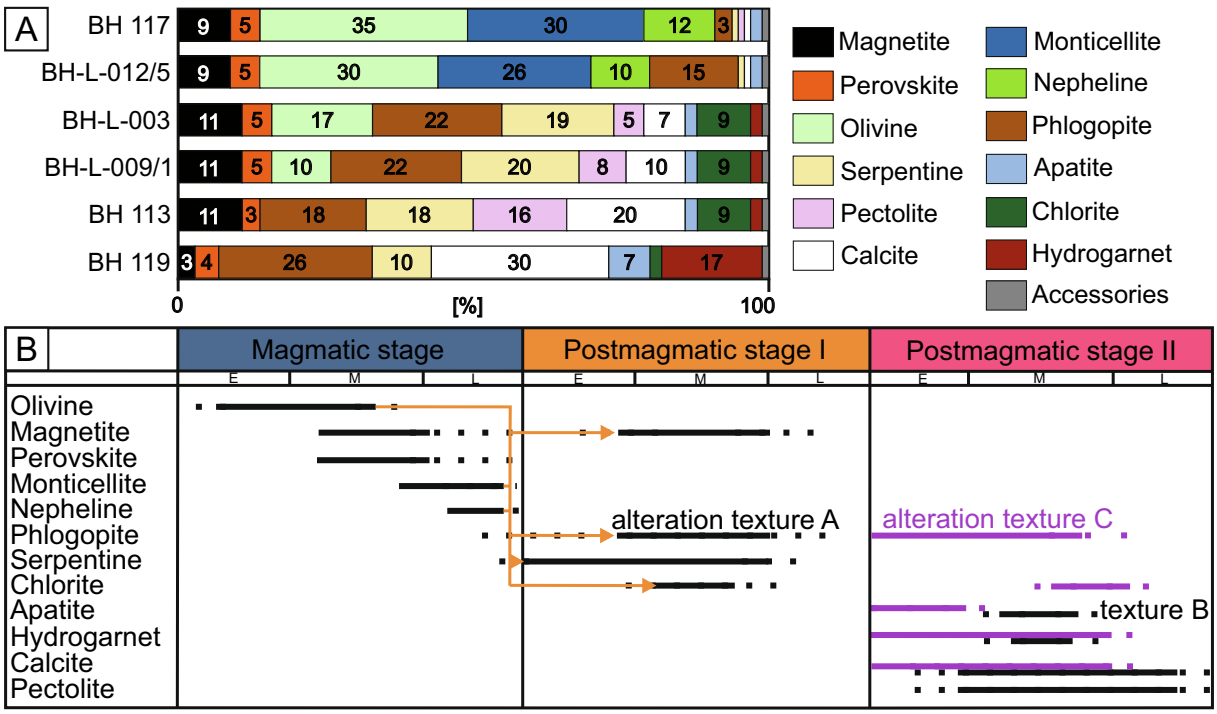

Fig. 3. A) Mineral modal % of the damtjernite samples (group 1) changing during the alteration process (from less to most altered), compared to a group 2 sample (BH119). B) Paragenetic sequences of the magmatic emplacement stage, alteration texture A (Postmagmatic stage I) and alteration textures B and C (Postmagmatic stage II). Purple sequences refer to crystallization only within alteration texture C. (For interpretation of the references to colour in this figure legend, the reader is referred to the web version of this article.)

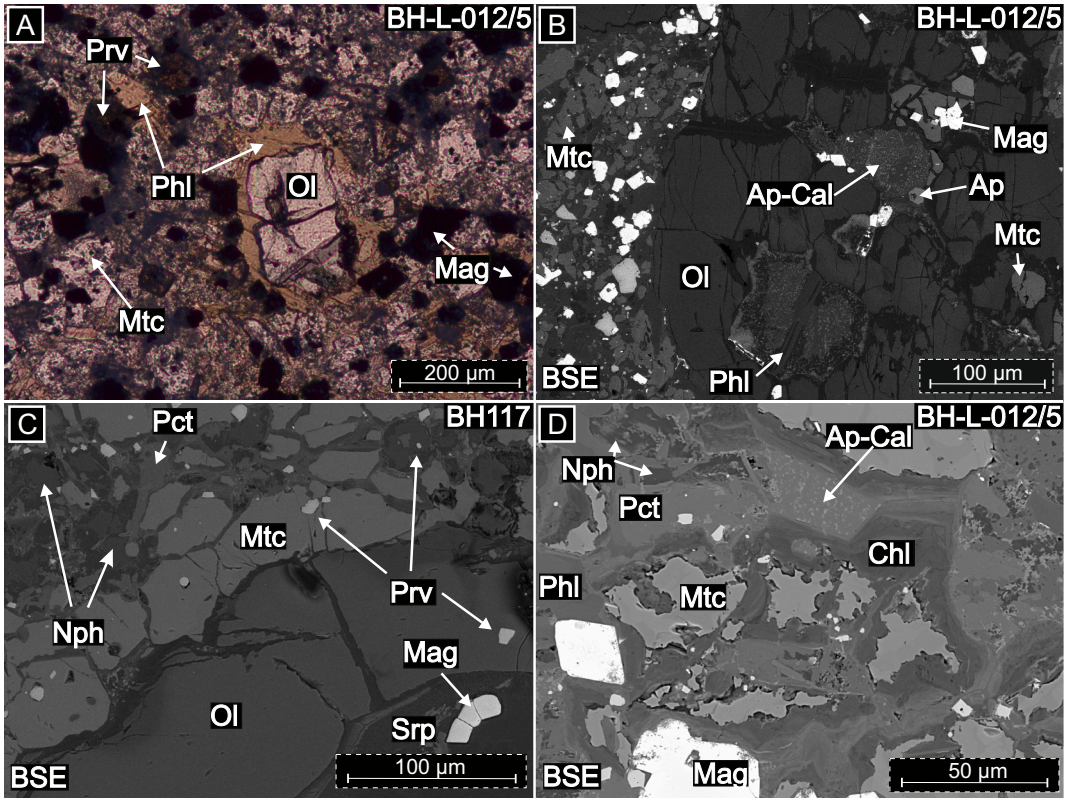

Fig. 4. Less altered damtjernites. A) Phlogopite grows around olivine microphenocryst. B) Apatite-calcite intergrowths and phlogopite within an olivine macrocryst. C) Olivine with perovskite inclusion as well as secondary magnetite and serpentine. Grainy groundmass of monticellite (with perovskite inclusions), nepheline and rare interstitial pectolite. D) Alteration of monticellite to chlorite. For mineral abbreviations see Fig. 2; Ap – apatite, Mag – magnetite, Mtc – monticellite, Nph – nepheline, Prv – perovskite, Chl – chlorite.

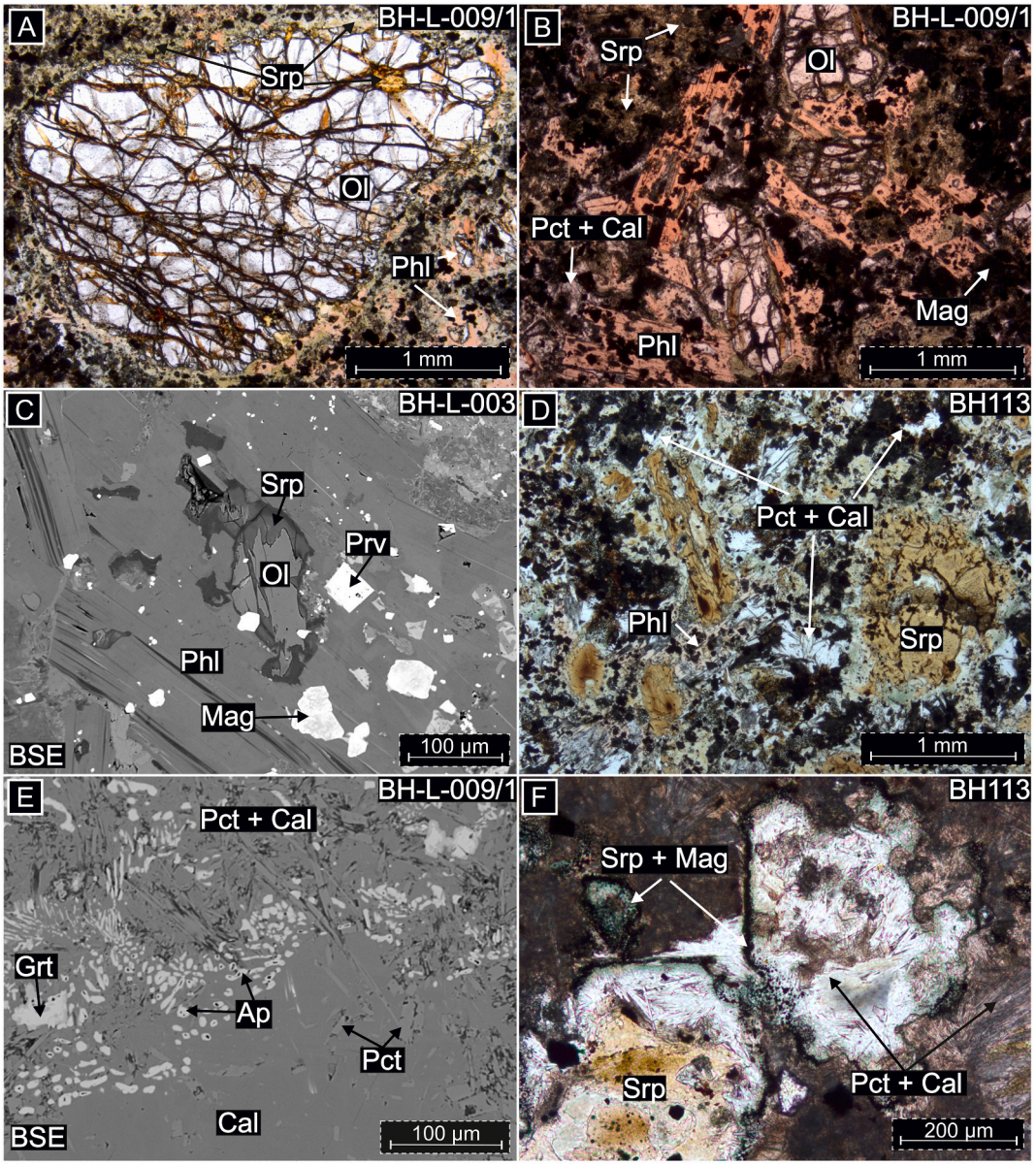

Fig. 5. Altered damtjernites. A) Residual (not completely serpentinized) olivine. Serpentine is filling the cracks and forming a green alteration rim. Secondary euhedral magnetite occurs in the cracks and on the alteration rim. B) Phlogopite macrocrysts grow around altered olivine and poikilitically include magnetite and perovskite. C) Small remnant of partially serpentinized olivine in poikilitic phlogopite. D) Secondary phlogopite and serpentine get replaced by pectolite and calcite intergrowth. E) Apatite-calcite intergrowth associated with garnet within pectolite and calcite. F) Pseudomorphs after serpentinized olivine, consisting of pectolite and calcite with relict serpentine in the core and remaining serpentine and magnetite alteration rim. For mineral abbreviations see Figs. 2, 4; Grt – garnet. (For interpretation of the references to colour in this figure legend, the reader is referred to the web version of this article.)

(Dolomite). SY-2 VF2 showed >90 % accuracy except for Zr, Nb, Tb, Dy, Ho, Er, Tm, Lu, Ta, Cr, Ni, Cu, Mo and Bi (>80 %). MEG-1 showed >90 % for most elements, except Nb, Th, Li, Cr, Co, Ni (>80 %) and Cu, Ag, Cd, Sb (errors up to 100 %). JDo-1 had >80 % accuracy with Sc, Zr, Hf, Ta, Li, Ti, V, Cu, Zn, Rb, Ag showing larger deviation, and Th was below detection.

3.5. Age dating

U—Pb dating of perovskite was conducted by LA-SF-ICP-MS at KIT using a Thermo-Scientific ELEMENT XR coupled to an Excimer Laser System (Teledyne Photon Machines Analyte Excite+), equipped with a two-volume cell (HELEX 100, EQC COMP, ANU Australia). Prior to dating, perovskite grains were imaged with a SEM (VEGA TESCAN system, backscattered electron mode) at 15 kV and < 10 nA. Detailed LA-SF-ICP-MS measurement and instrument conditions are in the Supplementary Data (Table B1). Instrumental drift was monitored and corrected using the reference glass NIST SRM-612 and matrix-match offset between glass and perovskite was addressed by measuring Afrikanda perovskite (371 ± 8 Ma; Reguir et al., 2010). Validation was done by analysing perovskite from the Gardiner carbonatite complex, yielding an age of 57.5 ± 3.2 Ma (n = 16; MSWD = 0.52), slightly older but overlapping within error with a published K—Ar phlogopite age of 53.9 ± 1.1 Ma (Noble et al., 1988). Data processing employed an in-house VBA spreadsheet program (Gerdes and Zeh, 2006, 2009).

In-situ (U-Th-Sm)/He age dating of apatite from the nearby Gross Brukkaros volcanic field was conducted at the Thermochronological Laboratory, University of Tübingen. This method is based on ^{4}He retention and diffusion produced by decay of ^{238}U, ^{235}U, ^{232}Th and ^{147}Sm (Ehlers and Farley, 2003; Farley, 2002). Calculation details are

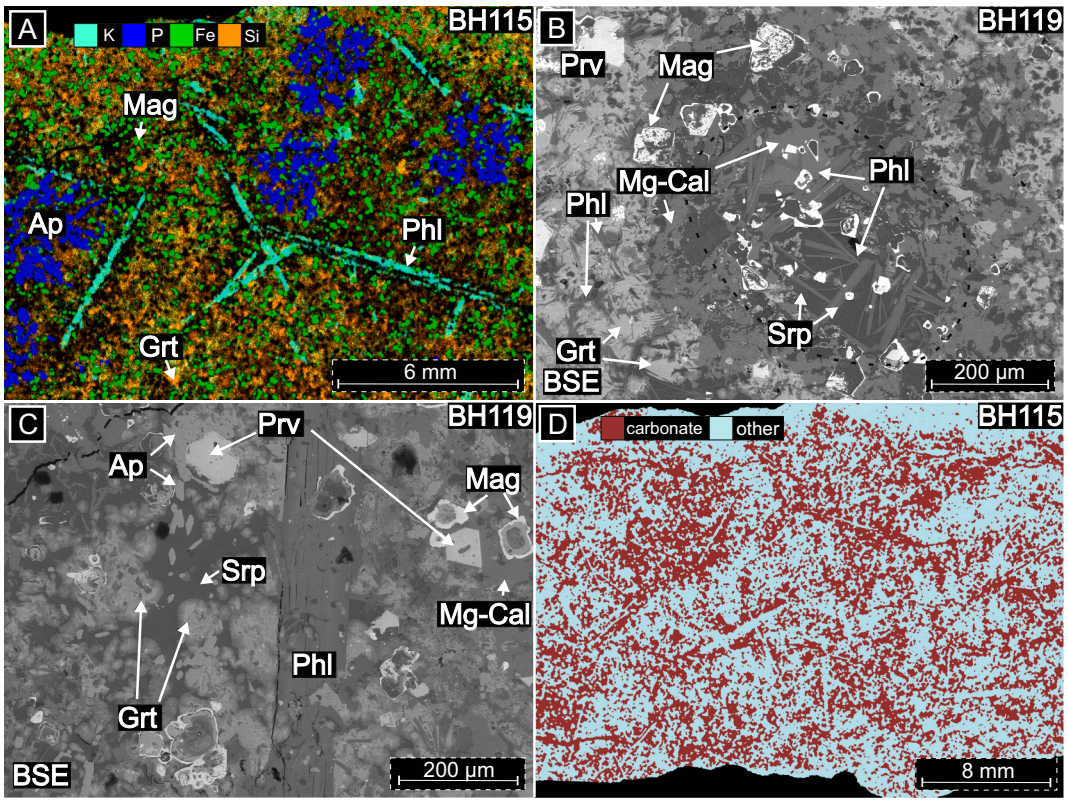

Fig. 6. Vein-like alteration of damtjernite. A) Clusters of apatite grains (dark blue) in a groundmass of magnetite (green) and garnet (orange). Macrocrystic phlogopites (turquoise) are well represented by K. B) Pseudomorph after olivine, consisting of phlogopite, calcite, serpentine and atoll-like magnetite. C) Concentric growth of garnet, euhedral apatite crystals and zoned magnetite pseudomorphs of compositions from chlorite to garnet. D) Distribution of calcite. For mineral abbreviations see Figs. 2, 4, 5. (For interpretation of the references to colour in this figure legend, the reader is referred to the web version of this article.)

provided in Farley (2002) or Glotzbach et al. (2010). Sample preparation involved crushing xenolith-free rock, magnetic separation, and hand-picking euhedral prismatic inclusion-free apatite grains following strict criteria (Farley, 2002). Grains were embedded in 1 mm thick PDA Teflon on glass mounts and polished for maximal surface area. Technical details on laser ablation, He analysis, and measurement configurations are in the Supplementary Data (Table B3). Laser ablation ICP-MS of trace elements (including U, Th, Sm) was performed at the center of each He ablation spot. NIST612 and Durango standards were used in a standard bracketing approach to estimate trace element concentrations (Paton et al., 2010). Outlier removal, background correction and concentration calculations were done with an in-house MATLAB app (ESD-U-Pb). ICP-MS results are in the Supplementary Data (Table B4). Laser pit volume was calculated from layered microscopic images, and internal MATLAB scripts were used for age determination. He-analysis results and final ages are documented in the Supplementary Data (Table B5).

4. Results

4.1. Petrography

Rock samples were gathered during fieldwork in 2019 including all previously classified picrites and the carbonate-phlogopite-apatite-pegmatite described by Kurszlaukis et al. (1999). Based on mineralogical and textural characteristics, three sample groups were identified (Table 1). Group 1 samples comprise abundant macrocrystic olivine, show a continuous evolution from less to strongly altered samples (Fig. 2A-C) and correspond to the three picrite types. Group 2 contains macrocrystic phlogopite (Fig. 2D) and corresponds to the carbonate-phlogopite-apatite-pegmatite. Group 3 represents variations of altered and brecciated country rock (Fig. 2E,F).

4.2. Group 1

Less altered magmatic rocks contain macrocrystic olivine within a fine-grained grey groundmass (Fig. 2A). Altered samples of the main complex show partially to fully serpentinized olivine embedded in a groundmass of greenish serpentine and phlogopite macrocrysts (Fig. 2B). In strongly altered samples, the groundmass is predominantly replaced by pectolite-calcite assemblages (Fig. 2C), which are less common in other samples (Fig. 2B).

The least altered samples (BH117, BH-L-012/5) are porphyritic with abundant olivine (Fig. 3A), minor magnetite macrocrysts (up to 4 mm) and microphenocrysts of olivine (150 µm – 1 mm), magnetite (up to 250 µm) and orange-brown perovskite (up to 250 µm; Fig. 4A). Olivine occasionally features inclusions of chromite grains and late crystallization of apatite-calcite intergrowth, that is hosted in its cracks (Fig. 4B) or interstitial to phlogopite within pseudomorphs after olivine. Rounded, polycrystalline olivine nodules also occur. The granular groundmass comprises a network of subhedral monticellite, anhedral nepheline (10-50 µm; Fig. 4C), and anhedral to subhedral phlogopite (100–600 µm; Fig. 4A). Magnetite inclusions appear in perovskite, whereas perovskite occurs in magnetite, olivine, and monticellite (Fig. 4C). In BH117, monticellite forms dense rims around olivine, contrasting with the more evenly distributed monticellite in BH-L-012/5. BH-L-012/5's groundmass features higher contents of light-brown phlogopite (100–600 µm), distributed uniformly or encompassing olivine (Fig. 4A). Olivine content decreases with increasing phlogopite. Groundmass phlogopite in BH117 is partly associated with chlorite, apatite and calcite as well (Fig. 4D). BH117 also contains sporadic 40 µm subhedral pectolite grains (Fig. 4C).

In more altered samples (BH-L-003, BH-L-009/1, BH113), two alteration textures are evident. Texture A comprises serpentine, magnetite, chlorite and phlogopite. Olivine is largely replaced by green

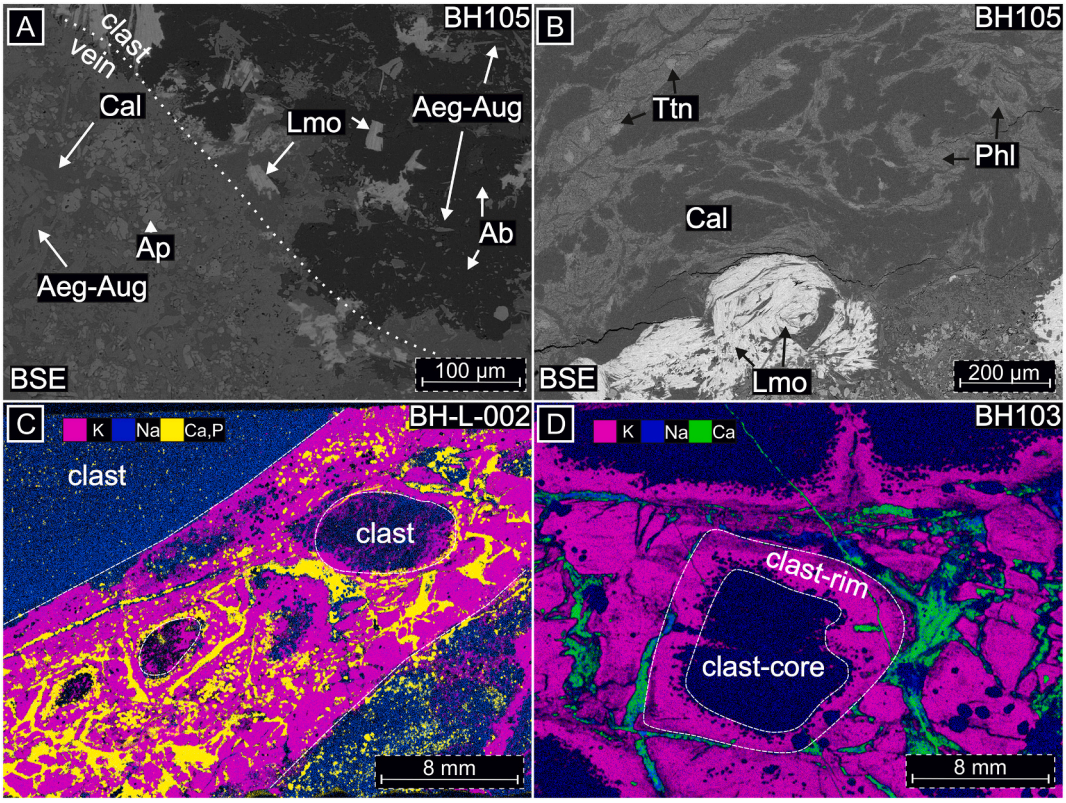

Fig. 7. Country rock breccias. A) Transition between an apatite- and calcite-rich vein and an albite-rich clast (fractured country rock). B) Lemoynite situated in a matrix of calcite-phlogopite intergrowth with minor titanites. C) Potassic brecciation zone intersected by apatite- and calcite-bearing veins. D) Diffuse K and Na zoning with sodic clast cores and potassic rims, as well as calcite-bearing veins. For mineral abbreviations see Figs. 2, 4; Lmo – lemoynite, Aeg-Aug – aegirine-augite, Ab – albite, Ttn – titanite.

and brownish serpentine and secondary magnetite (~50 µm; Fig. 5A). The groundmass is dominated by serpentine, chlorite, and poikilitic phlogopite (100 µm – 2 mm; Fig. 5B), with the latter containing resorbed cores of partially serpentinized olivine (Fig. 5C). Texture B shows needle-like pectolite (up to 500 µm; Fig. 5D,F) embedded in calcite, sometimes radially arranged, that is associated with apatite–calcite intergrowth similar to the less altered samples and minor amounts of hydrogarnet (up to 80 µm; Fig. 5E). Both alteration textures are concentrically arranged by intensity to the center of the complex (Fig. 1C). Due to replacement of serpentinized olivines by pectolite-calcite, frequently surrounded by a residual serpentine-magnetite alteration rim and encasing a remaining core of serpentinized olivine, as well as the interstitial relation between apatite-calcite and phlogopite, texture B appears to be younger than texture A.

4.3. Group 2

Group 2 samples host the third type of alteration texture at the Blue Hill (vein-like alteration; texture C) and intersect the complex at several localities (Fig. 1C). A key difference to the group 1 samples is the lack of macroscopically visible olivine. Colourless, platy phlogopite, embedded in a fine-grained greenish groundmass, appears more elongated than that in group 1 (Fig. 2D). Pseudomorphs after olivine up to 1 mm occur, containing tabular phlogopite, anhedral calcite, secondary magnetite and interstitial serpentine (Fig. 6B). Further, the distribution, habit and size of magnetite and perovskite microphenocrysts are very similar to group 1 samples. The samples contain abundant euhedral phlogopite, up to 2 cm in size (Fig. 6A), partly hosting magnetite and perovskite inclusions. Magnetite in BH119 exhibits atoll textured pseudomorphs (Fig. 6B,C), with a magnetite rim around fine-grained and zoned mixtures of serpentine, chlorite and calcite. In contrast, perovskite is mostly unaltered (Fig. 6C). Subhedral to euhedral apatite (~40 µm) forms dense aggregates of several mm within a serpentine groundmass (Fig. 6A,C). The groundmass comprises serpentine, hydrogarnet, phlogopite (~40 µm), anhedral calcite (up to 400 µm; Fig. 6D) and occasional chlorite (~50 µm). Hydrogarnet and phlogopite are associated within the groundmass (Fig. 6B), while textures of spheroidal hydrogarnet embedded in serpentine are also common (Fig. 6C).

4.4. Group 3

Country rock breccias at the Blue Hill range from unsorted matrix-supported (Fig. 2E) to slightly brecciated clast-supported samples (Fig. 2F) and colours from orange-brown to green-blueish. Grain sizes in both, clasts and groundmass, are extremely fine. The country rocks gradually transition in colour from red to blueish grey towards the Blue Hill. Altered samples (BH-L-002, BH105, BH108) are brecciated, with fine-grained clasts composed of albite, orthoclase, baryte, phlogopite, apatite and magnetite. Most of these minerals also occur in the fine-grained matrix, although calcite and euhedral aegirine-augite needles (up to 150 µm) are exclusively hosted in the matrix (Fig. 7A). Subhedral magnetite (up to 40 µm) is present throughout BH108. Samples BH-L-002 and BH105 contain lemoynite ($(Na,K)_2CaZr_2Si_{10}O_{26}{\cdot}5–6H_2O$), a transitional ino-phyllosilicate (Fig. 7A,B) forming aggregates up to 800 µm in veins and matrix. Accessory minerals include quartz, strontianite, titanite and rutile. In BH105, blueish grey clasts are albite-dominated (Fig. 7A), while the brown clasts in BH108 are rich in orthoclase. BH105 also features curved fibrous zones of colourless calcite and orange-brown phlogopite intergrowth, sometimes enclosing titanite grains (up to 40 µm; Fig. 7B) or lemoynite. Veins of calcite, apatite and albite (sometimes quartz) crosscut the matrix. Micro-XRF maps commonly show alkali zonation with Na-bearing clast cores, correlating

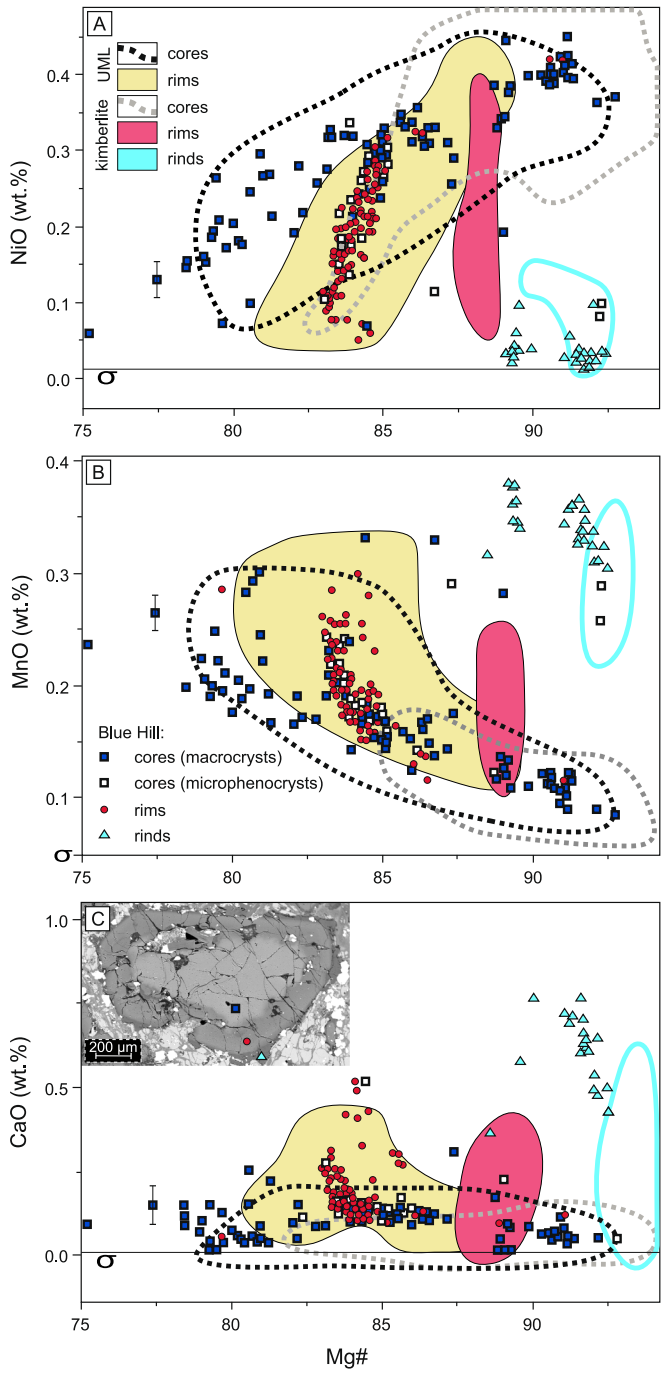

Fig. 8. Mineral chemistry of olivine at the Blue Hill compared to data of kimberlite and UML olivine. UML data by Veter et al. (2017). Kimberlite data by A) Mitchell et al. (2019) and references therein. B, C) Giuliani (2018) after Giuliani et al. (2017); Soltys et al. (2018); Nielsen and Sand (2008). Detection limits are given at σ. (For interpretation of the references to colour in this figure legend, the reader is referred to the web version of this article.)

with albite distribution (Fig. 7C,D). In some cases, the enrichment of K is confined to the brecciation zone around the country rock clasts (Fig. 7C), while in others, it is localized at the rims of clasts (Fig. 7D). The mineralogy of the brecciated country rock samples resembles typical fenites.

4.5. Mineral compositions

Olivine ranges from $Fo_{94}Fa_{06}$ to $Fo_{74}Fa_{26}$ (Fig. 8, Table 2 and Supplementary Data A8). NiO is higher in the cores (up to 0.45 wt%), while Ca is typically higher in olivine rims. High Mg# (~90–92) rinds with low NiO and high MnO (up to 0.39 wt%) and CaO (up to 0.75 wt%) are common. Olivine formula calculations are based on four oxygens.

Micas are Ti-bearing phlogopites (X_{Mg} of 77–94; up to 2.22 Ti p.f.u.), with enrichment of Al (up to 17.24 wt%) and Ba (up to 4.66 wt% BaO) in alteration texture C (Fig. 9, Table 3 and Supplementary Data A9). Additionally, only the micas in texture C exhibit a zoning along the c-axis (Fig. 9F), that shows enrichment of Al and Ba towards the rim, particularly in an intermediate zone, with this enrichment showing a positive correlation with *F. Mica* formula calculations are derived from the ideal trioctahedral mica formula ($XY_3[Z_4O_{10}][OH,F,Cl]_2$) with data normalized to 11 oxygens and 8 cations.

Perovskite is Na-poor (<5 mol% of loparite; up to 0.03 p.f.u. Na) and contains generally <5 wt% REE oxides (Supplementary Data A10), with no clear differences between different sample types, indicating the crystallization of all perovskite in equilibrium with the same melt. For perovskite, formula calculations are based on three oxygens.

Carbonate in the group 1 samples is purely calcite, whereas alteration texture C (group 2) exhibits Mg enrichment in calcite up to 4.3 wt % (Fig. 10A, Supplementary Data A11). Mineral formulas are normalized to 3 oxygens and 1 cation.

Spinel is mostly magnetite (Fig. 10B), though minor chromite is also present, always occurring as inclusions in olivine. Compositions reach up to 34.39 wt% Cr_2O_3 in chromite (see spinel-series in Fig. 10B, 0.97 a.p.f.u.) and 14.56 wt% TiO_2 (0.45 a.p.f.u.). Al_2O_3 contents are lower, up to 10.07 wt% (0.42 a.p.f.u.), while MgO reaches 11.93 wt% (0.62 a.p.f.u.). MnO remains below 1.36 wt% (0.06 a.p.f.u.). Fe^{2+} and Fe^{3+} reach up to 0.95 and 1.92 a.p.f.u., respectively (Supplementary Data A12). Spinel formula calculations are based on four oxygens.

Garnets yield constantly low analytical totals of ~95 % and show a slight anisotropy, which lead to the suspicion that they contain some OH (Cesare et al., 2019). This assumption was confirmed by Raman spectra that detected significant OH in the structure, based on bands around ~3684 cm^{-1} (Supplementary Data A13). Due to the general absence of an over-occupation of the octahedral site in analyzed garnets, the incorporation of Al^{3+} or Fe^{3+} on the tetrahedral site is not considered. Furthermore, an Fe^{2+} occupation on the dodecahedral site is excluded, as this position was originally over-occupied by Ca^{2+}. These estimations were necessary to reduce the variables on the tetrahedral position to one (H^+). Finally, the goal-seek function of EXCEL was used to determine the amount of H_2O (wt%) in the analyses to bring the dodecahedral site down to an occupation of 3. It was checked that the cation occupation of the tetrahedral site never exceeds the maximum occupation that is depended on the individual amount of H_2O and therefore H^+ in the analysis (T_{max} [a.p.f.u.] = Si^{4+}+(3-Si^{4+}) × 4). Based on this, garnets are andradite-grossular solid solutions with a hydrogarnet component. Water contents reach up to 4.11 wt% which corresponds to 2.17 a.p.f.u. H^+.

4.6. Whole rock analyses

Whole rock analyses (Table 4 and Supplementary Data A14) indicate depletion in MgO (down to 14.3 wt%), TiO_2 (to 1 wt%), and P_2O_5 (to 0.15 wt%), accompanied by enrichment in Al_2O_3 and CO_2 (both up to 7 wt%). CaO and SiO_2 remain relatively constant, whereas Na_2O and K_2O fluctuate irregularly. Group 2 demonstrates distinctly lower Na_2O (0.1 wt%), MgO (12.3 wt%) and SiO_2 (25.1 wt%), with significantly higher CaO (21.5 wt%) and P_2O_5 (1.27 wt%). Its CO_2 content (5.5 wt%) is comparable to the more altered group 1 rocks.

The country rock samples (two breccias; BH105, BH108 and one unaltered rock; BH107) exhibit a wide compositional variability. SiO_2 is depleted in brecciated samples, reduced to nearly half of the unaltered content (69.3 wt%). Na_2O and K_2O show no consistent trends: BH105 is enriched in Na_2O (9 wt%) and depleted in K_2O (0.7 wt%), while BH108 contains nearly equal amounts of both (5 wt% Na_2O, 5.5 wt% K_2O).

Table 2
Representative EPMA analyses for mineral chemistry of olivine at the Blue Hill.

Description	Less altered group 1	Less altered group 1	Less altered group 1	Less altered group 1	Altered group 1	Altered group 1	Altered group 1	Altered group 1
Sample	BH101	BH117	BH101	BH117	BH-L-009/1	BH-L-003	BH-L-009/1	BH-L-003
Analysis	Rim	Rim	Core	Core	Rim	Rim	Core	Core
wt%								
SiO_2	39.24	39.23	38.00	39.18	39.34	38.76	38.30	40.25
TiO2	0.00	0.04	0.00	0.00	0.03	0.00	0.00	0.00
Al2O3	0.03	0.01	0.00	0.02	0.02	0.03	0.00	0.02
FeO	14.20	15.34	19.02	14.54	15.04	14.02	17.90	9.11
MnO	0.18	0.25	0.19	0.17	0.19	0.17	0.29	0.12
MgO	45.15	44.38	40.85	44.84	44.59	44.83	41.95	49.42
CaO	0.11	0.21	0.00	0.12	0.11	0.11	0.04	0.05
NiO	0.31	0.14	0.19	0.25	0.21	0.30	0.00	0.40
Cr_2O_3	0.05	0.04	0.00	0.03	0.04	0.05	0.00	0.02
total	**99.28**	**99.64**	**98.29**	**99.16**	**99.58**	**98.27**	**98.49**	**99.40**
apfu								
Si^{4+}	0.992	0.993	0.993	0.993	0.994	0.990	0.992	0.992
Ti^{4+}	0.000	0.001	0.000	0.000	0.001	0.000	0.000	0.000
Al^{3+}	0.001	0.000	0.000	0.001	0.001	0.001	0.000	0.001
Fe^{2+}	0.300	0.325	0.416	0.308	0.318	0.299	0.388	0.188
Mn^{2+}	0.004	0.005	0.004	0.004	0.004	0.004	0.006	0.003
Mg^{2+}	1.702	1.674	1.591	1.694	1.680	1.707	1.620	1.816
Ca^{2+}	0.003	0.006	0.000	0.003	0.003	0.003	0.001	0.001
Ni^{2+}	0.006	0.003	0.004	0.005	0.004	0.006	0.000	0.008
Cr^{3+}	0.001	0.001	0.000	0.001	0.001	0.001	0.000	0.000
total	**3.009**	**3.007**	**3.007**	**3.008**	**3.006**	**3.011**	**3.008**	**3.008**
Mg#	0.850	0.838	0.793	0.846	0.841	0.851	0.807	0.906

Group 1 trace element concentrations generally decline with alteration, showing an average 57 % reduction from the least altered (BH117) to the most altered sample (BH113). The least altered sample shows notable contents in Zr (~300 ppm), Nb (~170 ppm), Ba (~790 ppm) and REEs: La (~160 ppm), Ce (~330 ppm), and Nd (~140 ppm). Negative anomalies in Ba, K, Pb, Zr, Hf, and Ti are evident in the spider-diagram (Fig. 11A). In the REE pattern (Fig. 11B) enrichment in LREEs is evident, while HREEs are relatively depleted. REE_{total} contents in group 2 are enriched by 14.3 % (average), when compared to the least altered sample of group 1.

4.7. Geochronology

Perovskite dating results are presented in the Tera-Wasserburg diagram (Fig. 12) and Supplementary Data (Table B2). The data show minor variations in $^{238}U/^{206}Pb$ and $^{207}Pb/^{206}Pb$ ratios and significant common Pb content. An unforced regression through all data ($n = 57$) yields a lower intercept age of 60 ± 14 Ma (MSWD = 1.1) at a low initial $^{207}Pb/^{206}Pb$ of 0.672 ± 0.063 (Y-intercept), well below values typical of Late Cretaceous to Tertiary (sub)volcanic rocks and xenoliths from depleted to enriched mantle sources (e.g. Fraser et al., 1985; Howarth et al., 2019; Zindler and Hart, 1986). Kimberlites from the Gibeon province show $^{207}Pb/^{206}Pb$ ratios of 0.79–0.82 (Davies et al., 2001). Using these data and anchoring the isochron at an initial $^{207}Pb/^{206}Pb$ of 0.80 ± 0.02 yields a lower intercept age of 83.6 ± 3.7 Ma, interpreted as the time of perovskite crystallization.

(U-Th-Sm)/He dating of 28 apatite spot analyses from a carbonatite dyke west of Gross Brukkaros yields a consistent mean age of 67.4 ± 8.7 Ma (Supplementary Data B5). Removing three outliers results in a slightly younger mean age of 66.1 ± 8.4 Ma. These outliers correspond to analyses with poor measurement statistics in the ICP-MS report, typically caused by suboptimal laser pit quality, which affects the accuracy of pit volume calculations for the helium analyses.

5. Discussion

The Blue Hill samples display a highly heterogeneous, but systematic alteration of the group 1 samples on a meter-scale (Fig. 1C, 14A), characterized by concentric alteration zones (Fig. 3, 14A). The outer zone, adjacent to surrounding rocks, shows only subtle alteration. Olivine remains mostly fresh, with minor secondary magnetite and serpentine in the cracks and occasional apatite-calcite intergrowths. Towards the center, olivine serpentinization intensifies and the primary assemblage is replaced by the large-scale alteration textures A and B. The later vein-like alteration texture C is (at least in todays outcrops) of minor volume compared to A and B, and is confined to the center and the edges of the magmatic body (Fig. 1C, 14A).

5.1. Classification of the primary intrusion

The typically primary nature of olivine macrocrysts (lacking xenocrystic cores) and the presence of primary pyroxene in picrites (Le Maitre et al., 2002) argue against classifying the group 1 samples as picrites, as previously done by Kurszlaukis et al. (1999). While volcanic rocks with 30–52 wt% SiO_2 and < 3 wt% $Na_2O + K_2O$ can still be chemically classified as picrites after TAS (>12 wt% MgO; Le Maitre et al., 2002), half the group 1 and 2 samples exceed 3 wt% $Na_2O + K_2O$ (Fig. 13A) and some fall below 30 wt% SiO_2. Additionally, the monticellite picrite and phlogopite-carbonate picrite described by Kurszlaukis et al. (1999) also exceed the 3 wt% threshold (Fig. 13A), while "mica-olivine-carbonate picrite" samples fall below the SiO_2 threshold. Macrocrystic olivine, phlogopite and primary nepheline establish the Blue Hill rocks as damtjernites according to the classification of Tappe et al. (2005). While recognizing primary carbonate minerals derived from the parental melt is difficult due to the extensive carbonate-bearing alteration of the complex, carbonate-bearing fenites support the presence of dissolved primary carbonate species in the melt. A parental UML melt agrees with mantle source estimates by Kurszlaukis et al. (1999) and Spriggs (1988), who proposed a source too shallow for a kimberlitic

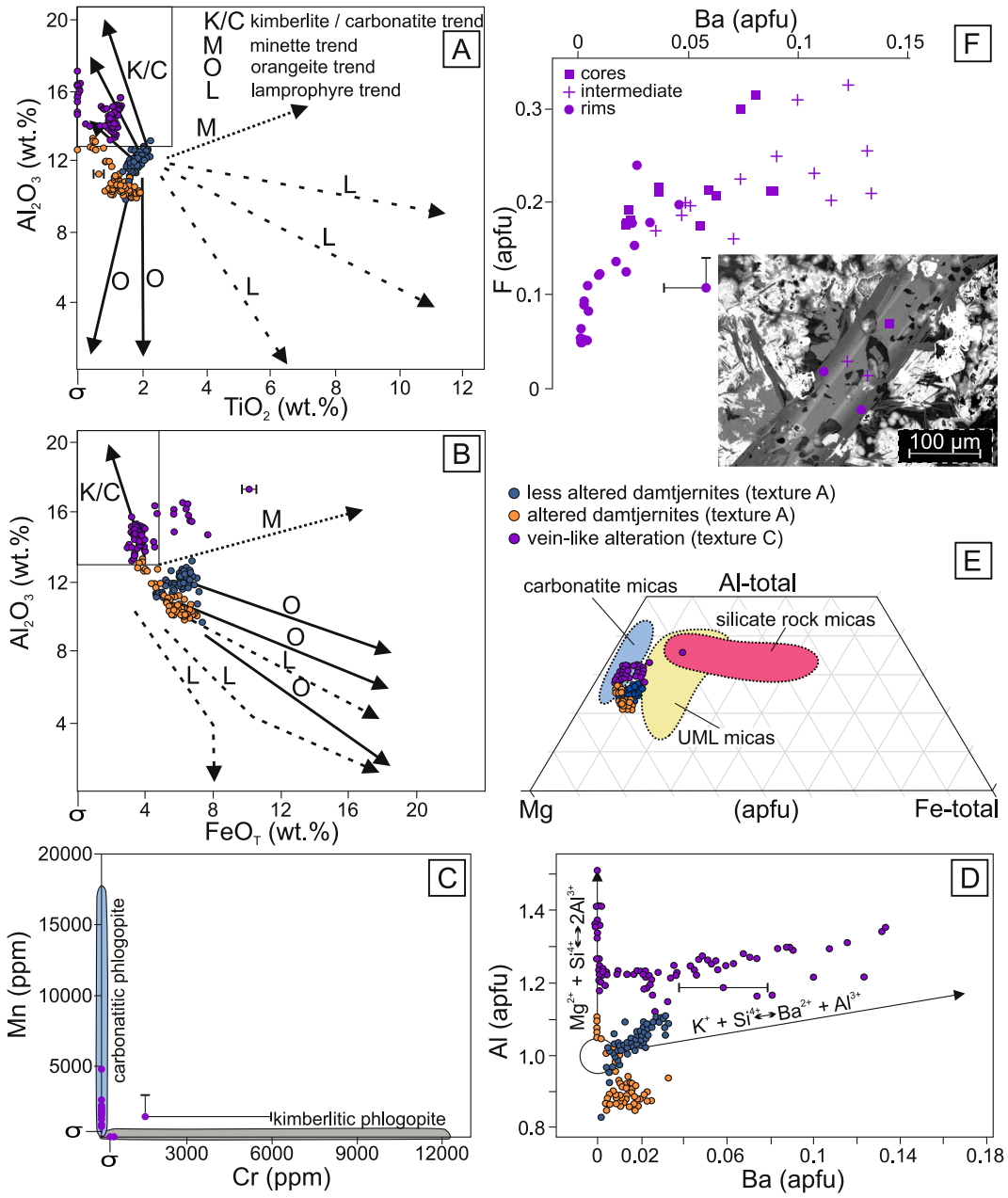

Fig. 9. Mineral chemistry of phlogopite at the Blue Hill. A, B) Al_2O_3 vs TiO_2 / FeO_{Total} plots with compositional trends for kimberlite-carbonatite, minette, orangeite and lamprophyre micas (Prokopyev et al., 2020 after Mitchell, 1995). C) Distinction between carbonatitic and kimberlitic micas via trace elements (Reguir et al., 2009). D) Al vs. Ba correlation after Giebel et al. (2019), showing various substitution mechanisms. E) Ternary Mg-Al-Fe diagram displaying compositions for carbonatite micas (Brod et al., 2001), UML micas (Dristas et al., 2013) and micas in more common magmatic silicate rocks (Brod et al., 2001). F) Zoning in phlogopites of texture C showing enrichment of Ba correlated to F. Standard deviation for Al does not exceed the symbol size. Detection limits are given at σ. (For interpretation of the references to colour in this figure legend, the reader is referred to the web version of this article.)

melt. UMLs, derived from the shallower cratonic lithospheric mantle, are consistent with this origin (Veter et al., 2017). A kimberlite classification would require crustal contamination to explain the high nepheline content (Smith et al., 2018), which is unlikely due to (1) the absence of crustal xenoliths or reaction halos and (2) the lack of primary clinopyroxene, typical in contaminated kimberlites (e.g. Smith et al., 1983). Although the high monticellite content is more characteristic of kimberlite, Abersteiner et al. (2018) suggest monticellite may form post-emplacement via CO_2 degassing, through reaction of dissolved carbonate ions in the melt with olivine. This could account for the dense monticellite rims around some olivine grains, as well as occasional monticellite in cavities of olivine (Fig. 4B). However, abundant

Table 3
Representative EPMA analyses for mineral chemistry of mica at the Blue Hill.

Description	Less altered group 1	Less altered group 1	Altered group 1	Altered group 1	Group 2	Group 2
Sample	BH-L-012/5	BH-L-004	BH-L-005	BH118	BH119	BH115
wt%						
SiO_2	39.71	39.83	41.86	42.21	37.32	38.27
TiO_2	2.04	1.76	1.36	0.78	1.32	1.17
Al_2O_3	12.65	11.47	10.36	12.73	15.20	14.14
Cr_2O_3	0.00	0.00	0.00	0.00	0.00	0.00
FeO	6.53	7.16	6.13	4.78	3.57	3.12
MnO	0.08	0.09	0.00	0.00	0.00	0.00
MgO	23.34	23.58	25.30	26.27	24.72	25.31
BaO	0.83	0.33	0.47	0.06	4.02	3.49
CaO	0.00	0.04	0.03	0.16	0.05	0.04
Na_2O	0.11	0.16	0.28	0.26	0.09	0.04
K_2O	10.14	10.09	9.98	10.15	9.06	9.37
F	0.85	0.76	1.15	0.06	0.87	1.34
Cl	0.00	0.00	0.00	0.00	0.01	0.00
total	**96.27**	**95.26**	**96.91**	**97.45**	**96.24**	**96.28**
apfu						
Na^{+}	0.015	0.022	0.039	0.035	0.013	0.005
Ca^{2+}	0.000	0.003	0.002	0.012	0.004	0.003
K^{+}	0.941	0.943	0.914	0.904	0.845	0.873
Ba^{2+}	0.024	0.009	0.013	0.002	0.115	0.100
Cr^{3+}	0.000	0.000	0.000	0.000	0.000	0.000
Fe_{tot}	0.397	0.439	0.368	0.279	0.218	0.190
Al^{3+}	1.085	0.990	0.877	1.047	1.310	1.217
Si^{4+}	2.889	2.917	3.006	2.947	2.728	2.794
Ti^{4+}	0.112	0.097	0.073	0.041	0.073	0.064
Mn^{2+}	0.005	0.005	0.000	0.000	0.000	0.000
Mg^{2+}	2.532	2.574	2.708	2.734	2.694	2.754
Cl^{-}	0.000	0.000	0.000	0.000	0.001	0.000
F^{-}	0.195	0.176	0.261	0.013	0.202	0.309
OH^{-}	1.805	1.824	1.739	1.987	1.797	1.691
total tetrahedron	**4.000**	**4.000**	**3.882**	**4.000**	**4.000**	**4.000**
total octahedron	**3.020**	**3.005**	**3.000**	**3.048**	**3.023**	**3.019**
total inter	**0.980**	**0.978**	**0.968**	**0.952**	**0.977**	**0981**

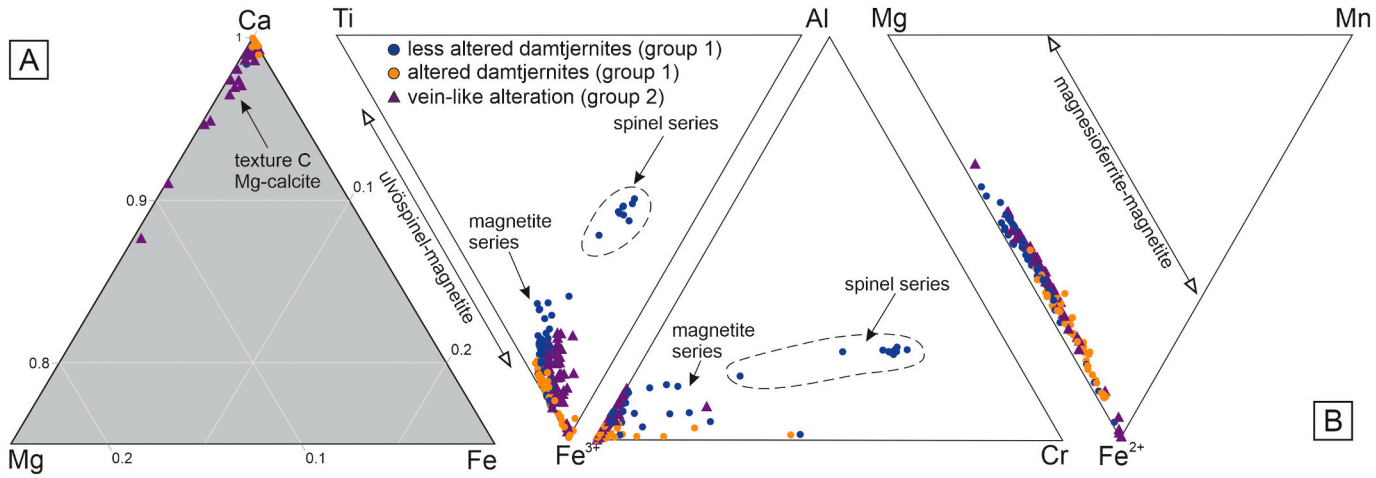

Fig. 10. A) Ternary Mg-Ca-Fe carbonate diagram showing a pure calcite composition in the group 1 damtjernites (texture B) and an evolution towards more Mg-rich compositions in group 2 (texture C). B) Mineral chemistry of spinel after Braunger et al. (2018). The compositions are dominated by Fe—Ti oxides plotting along the ulvöspinel-magnetite line. Secondary magnetite from the altered damtjernites exhibits typical magnetite compositions. A distinct trend shows Cr- and Al-rich compositions (e.g. chromite) that represent inclusions within olivine cores.

inclusions of small perovskite grains (Fig. 4C) still indicate magmatic or late-stage monticellite crystallization. Whole-rock major and trace element data from group 1 and 2 samples mostly plot within the compositional range of UMLs (Fig. 13B and Supplementary Data A15), though a better fit to kimberlite-like compositions is seen in TiO_2 and Zr/Nb. The incompatible trace element spider diagram (Fig. 11A) shows high similarity to UMLs from the Torngat Mountains (Canada), except for the most altered group 1 sample, which aligns more with kimberlite compositions. The REE pattern of Blue Hill differs from that of kimberlites (particularly HREEs) and matches damtjernites from Kutch

Table 4
Whole rock major and trace element composition for the Blue Hill.

Description	Less altered group 1	Less altered group 1	Altered group 1	Altered group 1	Group 2	Country rock breccia	Country rock breccia
Sample	BH117	BH-L-012/5	BH-L-009/1	BH113	BH119	BH105	BH108
wt%							
Na_2O	1.95	0.88	1.41	1.14	0.13	8.99	5.03
MgO	20.10	18.63	14.25	16.70	12.34	3.56	3.57
Al_2O_3	5.27	4.91	6.94	6.95	5.11	12.94	14.78
SiO_2	31.19	28.80	30.06	31.42	25.13	42.43	52.44
P_2O_5	0.33	0.82	0.42	0.15	1.27	1.19	0.45
K_2O	1.26	1.56	2.49	1.60	1.59	0.71	5.51
CaO	15.88	15.75	14.99	15.87	21.54	12.26	4.07
TiO_2	3.28	3.26	3.01	0.98	3.48	0.79	0.79
MnO	0.29	0.26	0.18	0.17	0.27	0.16	0.11
FeO_{total}	16.74	15.73	13.72	10.03	15.16	5.91	6.88
L.O.I.	2.65	5.45	9.41	14.09	13.18	9.69	4.45
total	98.93	96.05	96.87	99.10	99.21	98.63	98.07
CO_2	0.98	2.03	4.62	6.94	5.54	4.93	0.93
SO_2	0.30	0.66	0.10	0.10	0.16	0.08	0.10
ppm							
Sc	26.05	24.15	19.82	12.38	26.49	16.16	17.22
Y	36.26	29.78	17.21	13.71	40.50	29.66	28.26
Zr	262.67	297.87	264.39	54.33	361.44	244.58	213.28
Nb	174.91	159.34	142.36	35.25	46.62	24.73	3.85
Ba	246.34	788.67	628.65	124.92	580.19	268.88	1185.55
La	159.76	144.90	132.26	41.59	196.53	37.56	29.47
Ce	332.57	286.22	267.83	84.46	399.64	76.15	59.59
Pr	37.98	32.19	30.42	9.60	45.46	9.07	7.02
Nd	140.62	117.74	112.22	34.68	167.28	36.07	26.57
Sm	23.04	19.23	18.04	5.43	27.52	7.07	5.66
Eu	6.06	5.09	4.54	1.34	7.27	1.34	1.07
Gd	15.75	13.17	11.58	3.66	18.77	5.72	5.04
Tb	1.91	1.59	1.31	0.48	2.24	0.83	0.83
Dy	9.00	7.36	5.61	2.46	10.28	4.71	4.98
Ho	1.47	1.19	0.81	0.46	1.64	0.97	1.04
Er	3.32	2.66	1.58	1.20	3.62	2.91	3.04
Tm	0.40	0.32	0.16	0.17	0.42	0.45	0.47
Yb	2.16	1.68	0.77	0.97	2.23	2.99	3.03
Lu	0.31	0.24	0.11	0.15	0.31	0.49	0.50
Hf	9.08	8.32	8.27	1.49	7.51	3.90	5.12
Ta	10.64	9.65	8.28	2.49	2.86	0.70	0.13
W	7.27	4.46	6.00	2.28	1.33	9.41	1.94
Th	22.51	20.21	22.59	8.55	25.59	11.82	15.48
Li	6.33	16.15	25.46	5.43	15.17	33.85	38.40
Be	1.46	2.68	2.97	0.86	1.58	4.25	2.76
Ti	21,868.68	22,246.72	20,022.84	6339.76	19,144.03	2905.85	3907.40
V	109.41	179.23	117.59	46.05	124.79	250.38	287.81
Cr	638.03	680.55	399.83	599.00	381.40	55.08	71.71
Mn	2278.44	2002.19	1391.17	1295.08	2172.48	1217.31	852.64
Co	79.29	75.00	60.57	59.13	54.61	20.03	17.38
Ni	337.57	343.96	231.40	331.63	84.73	30.97	33.89
Cu	47.84	70.43	22.55	29.42	127.70	61.11	35.38
Zn	95.78	101.48	108.52	107.66	90.70	90.52	96.26
Rb	37.45	66.12	83.00	46.18	50.80	48.81	191.16
Sr	607.22	1001.41	879.00	579.98	760.79	790.61	389.25
Mo	1.16	1.71	0.20	0.12	0.72	2.55	0.75
Ag	0.17	0.22	0.17	0.05	0.17	0.09	0.07
Cd	0.12	0.15	0.07	0.08	0.23	0.18	0.12
Sb	0.05	0.15	0.24	0.84	0.13	0.36	0.21
Cs	0.22	0.83	2.49	1.95	1.28	2.07	40.43
Pb	2.79	5.54	2.84	2.05	7.44	21.71	23.35
Bi	0.02	0.03	0.02	0.02	0.04	0.24	0.30
U	4.00	3.74	3.99	1.43	5.96	57.65	3.70

(India; Fig. 11B).

Olivine analyses (cores and rims) consistently lie within UML compositional ranges (Fig. 8), though some high Mg# rinds (with low NiO, but4;lk high CaO and MnO) overlap with those from kimberlites (Giuliani, 2018). Olivine rinds in kimberlites are typical for equilibrium crystallization with carbonate-rich residual melts (high oxygen fugacity prevents incorporation of Fe^{2+} in olivine) at emplacement level (Mitchell et al., 2019). Similar olivine rinds may also form in UMLs as these melts contain primary dissolved carbonate, which is believed to produce high Mg# rinds (Giuliani, 2018; Mitchell et al., 2019). The narrow Mg# range of rims resembles that in kimberlites, possibly indicating a similar ascent mechanism via assimilation-fueled buoyancy (Russell et al., 2012). Rounded macrocrysts may reflect mechanical abrasion during ascent, whereas subhedral to euhedral

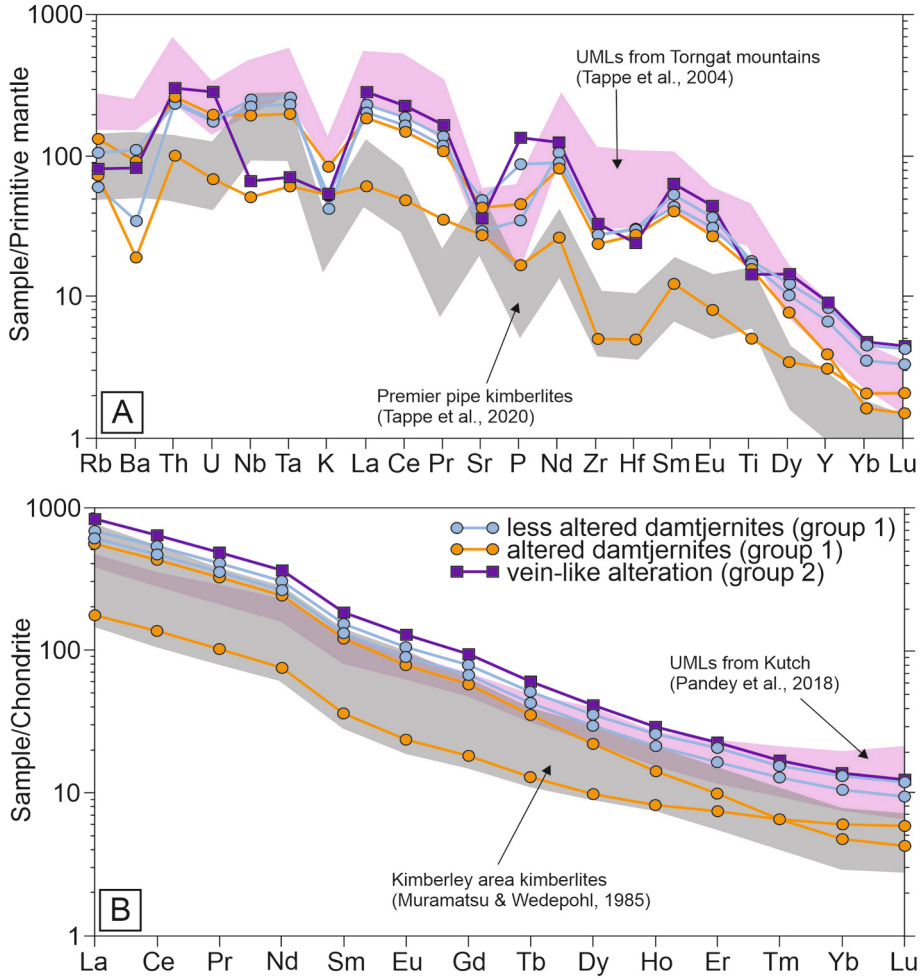

Fig. 11. (A) Normalized trace element / primitive mantle spider diagram and (B) REE / chondrite pattern (primitive mantle and chondrite data after Sun and McDonough, 1989; Lodders and Fegley, 1998) compared to premier pipe kimberlites (Tappe et al., 2020) and UMLs from the Torngat mountains (Tappe et al., 2004), as well as the REE composition fields of kimberlites from the Kimberley area (Muramatsu and Wedepohl, 1985) and damtjernites from Kutch, northwestern India (Pandey et al., 2018).

microphenocrysts and macrocryst rims likely crystallized during ascent and emplacement. This is supported by some microphenocryst cores following rim trends in Fig. 8. Chromite and Cr-rich spinel inclusions hosted in olivine cores show a distinct trend in Fig. 10B, which goes in line with a mantle-derived origin for the xenocrystic olivine cores.

5.2. *Multiphase alteration stages in the UML and its country rocks*

5.2.1. *Alteration texture C*

Group 2 rocks hosting alteration texture C (formerly carbonate-phlogopite-apatite pegmatite) have been interpreted as in-situ differentiation products of the magmatic body (Kurszlaukis et al., 1999). The term "pegmatite" is inadequate, as phlogopite is the only coarse-grained phase, hosted in a fine- to microcrystalline matrix of phlogopite, apatite, carbonate, serpentine and hydrogarnet (Fig. 6). The presence of olivine pseudomorphs (Fig. 6B), similar distribution, habit and size range of perovskite and magnetite (strongly altered; Fig. 6B,C), along with abundant hydrogarnet, Mg-calcite and apatite, suggest group 2 to represent a metasomatic alteration product of the more pristine magmatic rocks. Analyses of perovskite show no compositional difference between different Blue Hill rocks, supporting a common primary crystallization environment and time.

Al_2O_3 vs. TiO_2 and FeO_{Total} relations show a clear distinction of micas from alteration texture C, that follow the kimberlitic/carbonatitic trend (Fig. 9A,B). Phlogopite compositions from kimberlites and carbonatites cannot be distinguished by major elements (Reguir et al., 2009), making the kimberlite and carbonatite fields interchangeable in such diagrams. The distinction in minor elements like Mn and Cr (Fig. 9C) allows to separate carbonatitic from kimberlitic micas.

Texture C micas further reveal kinoshitalite substitution ($K^+ + Si^{4+} = Ba^{2+} + Al^{3+}$; Giebel et al., 2019; Fig. 9D), indicating Ba- and Al-enrichment relative to micas from alteration texture A. This requires an external Ba source, consistent with a carbonatitic influence, as carbonatites are commonly Ba-bearing (e.g. Anenburg and Mavrogenes, 2018; Li et al., 2020; Von Knorring, 1962 and references therein). The Mg-component in calcite (Fig. 10A), the large content of euhedral apatite grains (Fig. 6) combined with the distinct phlogopite chemistry showcase the carbonatitic affinity of this alteration stage. Whole-rock data supplements this hypothesis, displaying a clear enrichment of REEs in the vein-like group 2 samples (Fig. 11B). The reaction between

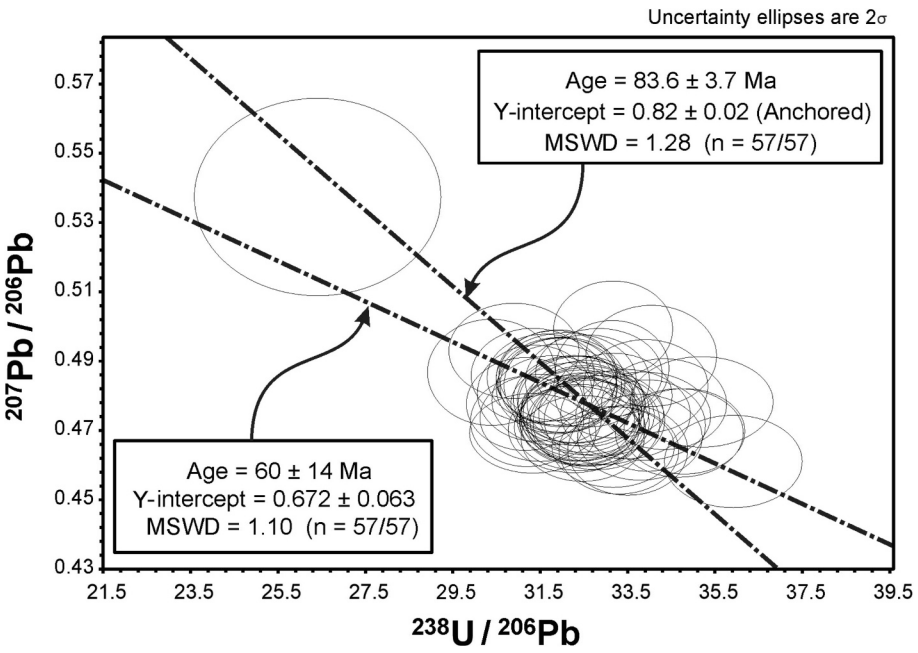

Fig. 12. Tera and Wasserburg (1972) U—Pb diagram for perovskite from group 1 damtjernites of the Blue Hill before and after anchoring the Y-intercept. Uncertainty ellipses are reported at 2σ (2 standard deviation uncertainties; Supplementary Data, B2). (For interpretation of the references to colour in this figure legend, the reader is referred to the web version of this article.)

olivine and a carbonatitic melt, with silica and aluminium supplied by nepheline, would produce phlogopite, serpentine, calcite, and excess CO_2, leading to a CO_2-rich residual fluid (Eq. 14). This interpretation is supported texturally by pseudomorphs after olivine in alteration texture C, which consist of phlogopite, serpentine, calcite and magnetite (Fig. 6B). The presence of magnetite can be attributed to redistribution of the fayalite component in olivine.

$$4SiO_2 + Al_2O_3 + 4H_2O + MgCa(CO_3)_2 + K_2CO_3 + 4Mg_2SiO_4 \rightarrow 2KMg_3(AlSi_3O_{10})(OH)_2 + Mg_3(Si_2O_5)(OH)_4 + CaCO_3 + 2CO_2. \quad (1)$$

silicium oxide + aluminium oxide + water + carbonatitic melt + olivine → phlogopite + serpentine + calcite + carbon dioxide.

5.2.2. *Alteration textures A and B*

Formation of alteration texture A (serpentine-magnetite-phlogopite-chlorite) appears to be isochemical. Mineral chemistry of spinel indicates that secondary magnetite, formed due to olivine alteration, especially in the altered damtjernites, tends to show a more pristine magnetite composition (Fig. 10B).

Alteration texture B (pectolite–apatite–hydrogarnet–calcite), which is texturally younger than texture A, shows multiple possible genetic origins. One model suggests that both textures derive from a common parental fluid, which becomes progressively enriched in carbonate (until saturation) as serpentine crystallization depletes OH, explaining the structural overlap of both alteration stages in a common origin (Fig. 14B, scenario 1). Potential fluid sources include late-stage magmatic (deuteric) or meteoric fluids. A comparable issue concerns serpentine crystallization in kimberlites. While serpentine was long considered deuteric (e.g. Mitchell, 1986), later studies (e.g. Giuliani et al., 2017; Sparks et al., 2009) argue for mixed fluids with a substantial meteoric component of external fluids. The abundant phlogopite forming together with serpentine at the Blue Hill indicates crystallization at elevated temperatures. In kimberlites, where meteoric fluids are likely too cool for phlogopite formation, phlogopite typically occurs as a primary phase (e.g. Giuliani et al., 2017) that is subsequently replaced by serpentine or chlorite (Mitchell, 1986). Therefore, at the Blue Hill, a dominant meteoric contribution to the fluids producing texture A is unlikely. Considering the phlogopite- and carbonate-bearing fenites, a parental fluid capable of stabilizing phlogopite and carrying dissolved carbonates for later calcite crystallization could plausibly originate from a late-magmatic residual phase of the damtjernite.

An alternative model would assign alteration textures A and B to genetically separate stages. Interstitial time-relations and pectolite-calcite (texture B) replacing serpentinized olivines (texture A; Fig. 5F) support this interpretation. In this case, spatial overlap of textures A and B the damtjernite complex reflects successive fluids exploiting the same

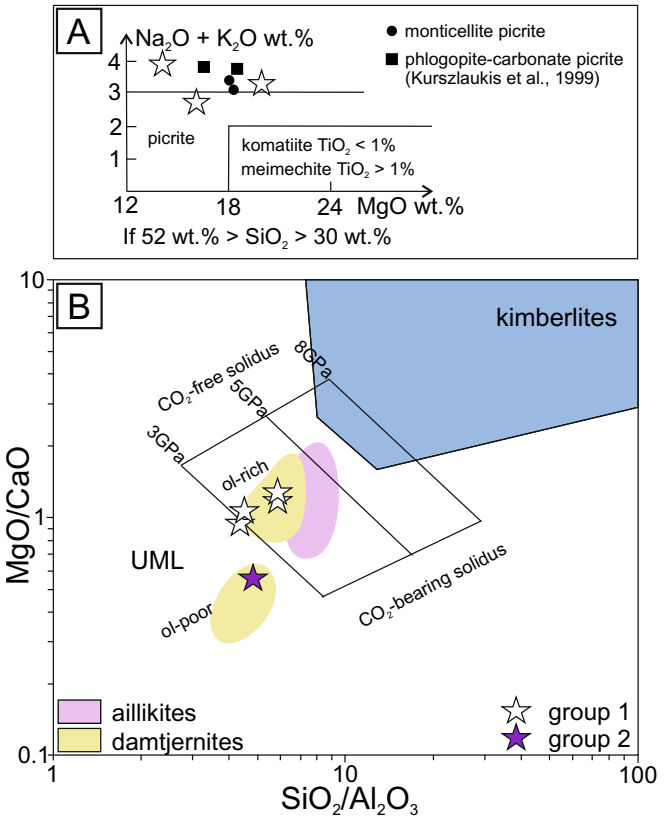

Fig. 13. A) "High-Mg" volcanic rocks after Le Maitre et al. (2002). Blue Hill samples with the required SiO_2 >30 wt% are plotted alongside monticellite and phlogopite-carbonate picrites (Kurszlaukis et al., 1999), while the mica-olivine-carbonate picrite does not reach this threshold. B) MgO/CaO vs. SiO_2/Al_2O_3 discrimination diagram of Tappe et al. (2006) after Rock (1991) with compositions for experimentally produced melts (3–8 GPa) from Gudfinnsson & Presnall (2005). Compositional fields for kimberlites, aillikites and olivine rich and poor damtjernites are compared with whole rock data of the Blue Hill. (For interpretation of the references to colour in this figure legend, the reader is referred to the web version of this article.)

pathways.

Texture B (pectolite–apatite–hydrogarnet–calcite) would thus represent a later fluid pulse, sharing features with the carbonatitic affinity of texture C (e.g. presence of apatite and similar garnet compositions to those in texture C). However, key differences exist: apatite in texture B is sparse, typically anhedral and usually forms segregation-like drops in calcite, whereas apatite in texture C is more abundant, euhedral and grainy (1.27 wt% P_2O_5 in group 2 vs. 0.43 wt% (mean value) in group 1). According to outcrop observations, the dimensions of texture C appear to be rather narrow and vein-like, while texture B follows the concentric pattern of the complex and is especially prominent in the center. Moreover, Mg-enrichment in calcite is restricted to texture C, although calcite in texture B is Mg-free.

If texture C originated from an external carbonatitic fluid (e.g. from Gross Brukkaros), texture B may reflect a later fluid pulse of modified composition reaching the Blue Hill (Fig. 14B, scenario 2). Alternatively, if texture C formed from a carbonatitic melt, the excess of CO_2 from the reaction between the melt and the damtjernite could be dissolved in the residual fluid (Eq. 1), which then initiated crystallization of texture B by utilizing the existing fluid pathways in the magmatic complex (Fig. 14B, scenario 3).

5.2.3. Fenitization

Whole-rock data reveals lightly brecciated sodic and strongly brecciated potassic fenite types, consistent with the distribution of Na-bearing minerals (e.g., albite, aegirine-augite) and K-bearing minerals (e.g. phlogopite, orthoclase). Micro-XRF mapping reveals two fenitization stages. Cores of fenitized clasts consistently exhibit higher Na contents, whereas breccia fillings or clast rims along breccia veins are enriched in K (Fig. 7C,D). This might suggest an initial sodic fenitization stage, followed by a subsequent potassic stage. As the fenites are in contact with the outer (less altered) damtjernite of the complex, they appear to be a product of hydrothermal fluids exsolved by the primary intrusion. Although, the high content of calcite- and apatite-bearing veins does not fit to the carbonate-poor damtjernite and might be correlated to the external carbonatitic liquids as well.

5.3. Geochronological evidence

The Tera-Wasserburg diagram yields an age of 60 ± 14 Ma and displays an unusually low Y-intercept, which may have multiple causes. Local radioactive decay can generate excess ^{206}Pb, lowering the $^{207}Pb/^{206}Pb$ ratio. For example, the Bingo alkaline-carbonatite complex shows a very low Y-intercept of 0.1554 for carbonatite, interpreted as pyrochlore recrystallization during intense laterization from a radiogenic source (Kasay et al., 2024). However, no such laterization is observed or inferred at Blue Hill, making it more likely that excess ^{206}Pb was introduced through metasomatic overprinting and therefore represents a resetting age. To correct for common lead in the Tera-Wasserburg plot, the Y-intercept is anchored to a more typical value, consistent with terrestrial Pb isotope evolution (Stacey and Kramers, 1975). Further, the uncorrected age of 60 ± 14 Ma overlaps with the 66.1 ± 8.4 Ma age for the Gross Brukkaros carbonatite, derived from (U-Th-Sm)/He apatite dating (see Supplementary Data B5), as prior U—Pb attempts failed due to high common lead. A 60 ± 14 Ma age for the metasomatic interaction therefore supports carbonatitic influence for the alteration of the main damtjernite body (textures A and/or B), where the dated perovskite grains are hosted. The age of 75.1 ± 0.6 Ma by Kurszlaukis (1994) provides constrains on the timing of alteration texture C as it was derived from phlogopite of the "carbonate-phlogopite-apatite-pegmatite" (group 2 samples in this study). The evolution of a single silicate-rich fluid beyond carbonate solubility, potentially producing textures A and B, conflicts with the resetting age. In this model, the late-magmatic fluids carrying dissolved carbonate ions that are the primary candidates for the parental fluid would be excluded by the way younger resetting age. Texture C predating the resetting age supports the intrusion of a carbonatitic liquid, possibly from Gross Brukkaros, before alteration texture B forms, whereas the resetting age itself likely records the last alteration of group 1 damtjernites, corresponding to texture B. The older corrected age of 84 ± 4 Ma therefore reflects the intrusion of the parental melt for the Blue Hill complex.

6. Conclusion

The Blue Hill complex most likely formed from an ultramafic lamprophyre (UML) melt. Distinct olivine zonations support a mantle origin of macrocryst cores, while post-emplacement degassing of dissolved carbonate is indicated by high-Mg# olivine rinds and monticellite reaction rims around olivine in the primary samples.

Three alteration stages (A, B, C) are recognized, each with distinct characteristics. Alteration textures A and B spatially overlap in group 1 damtjernite samples (both concentrically arranged), whereas texture C occurs as crosscutting veins throughout the complex. Texture A points to an isochemical alteration reaction by a mix of deuteric or meteoric fluids, with the excessive crystallization of phlogopite indicating a dominant part of deuteric (late-magmatic) fluids due to a higher crystallization temperature. Contrary, in kimberlites where a higher proportion of meteoric fluids in presumed, serpentine and chlorite also form, but phlogopite is typically not part of the alteration assemblage. In contrast, texture C shows a clear carbonatitic affinity, featuring carbonatite-like whole-rock compositions, typical Al- and Ba-rich

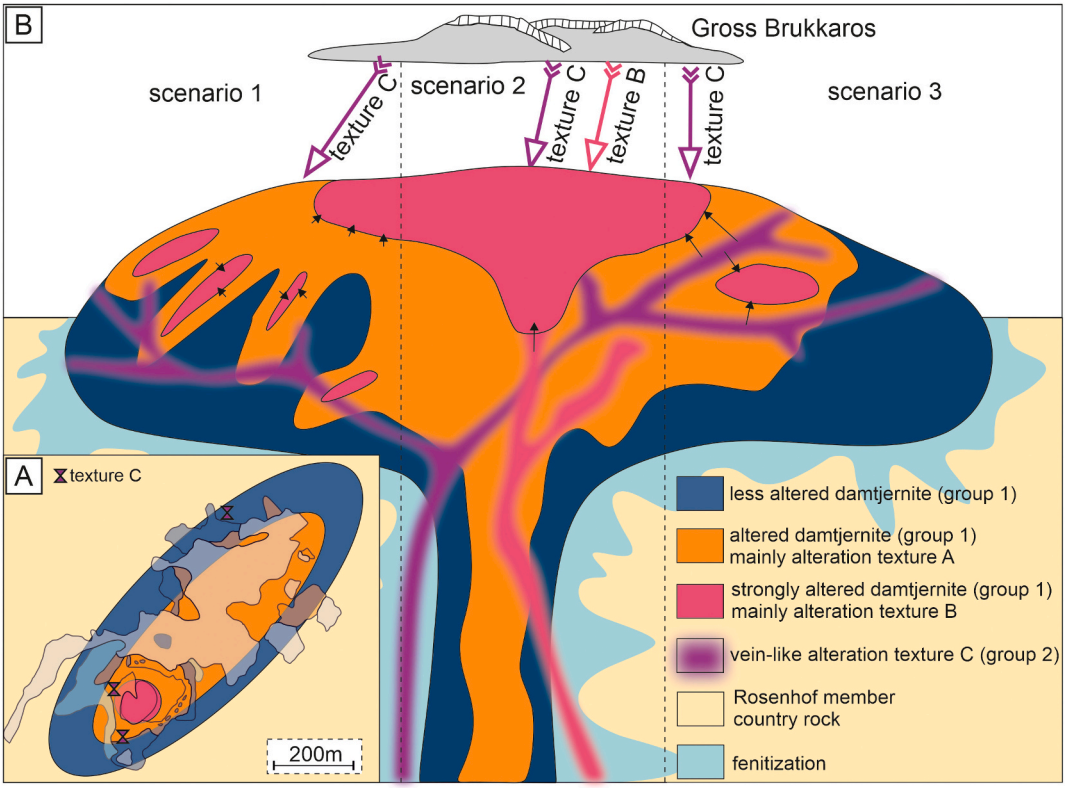

Fig. 14. A) Simplified plan view of the Blue Hill showing alteration zones within the complex. B) Schematic cross-section model of the Blue Hill complex (not to scale). A pulse of carbonatitic liquids, possibly derived from Gross Brukkaros, is assumed for all three scenarios (texture C). Alteration texture A is isochemical and fits to a mix of late-magmatic and meteoric fluids. Texture B could be derived from (1) evolution of the late-magmatic liquids until saturation of carbonate, (2) a later pulse of external carbonatitic fluids or (3) from CO_2-rich residual fluids of alteration texture C. (For interpretation of the references to colour in this figure legend, the reader is referred to the web version of this article.)

phlogopite chemistry (discriminated by kimberlitic micas via Mn vs. Cr), Mg-rich calcite and large quantities of apatite. The genetic relationship of texture B remains more complex. While it could theoretically evolve from the same residual fluid as texture A by depleting OH and enriching carbonate ions until saturation, geochronology indicates a time gap of at least 6 Ma between magmatic emplacement (84 ± 4 Ma) and the resetting age (60 ± 14 Ma), rendering such an origin unlikely. Instead, texture B likely represents a later fluid pulse. Its mineralogical similarities to texture C (apatite, hydrogarnet) but distinct textural and chemical features (anhedral vs. euhedral apatite; Mg-free vs. Mg-rich calcite) could suggest formation from a CO_2-rich residual fluid derived from texture C. This is in agreement with the geochronology as the resetting age is younger than the age of alteration texture C, although a later pulse of carbonatitic fluids independent to texture C cannot be excluded.

More broadly, this study demonstrates that age dating and mineral chemistry are critical tools to distinguish genetically separate carbonatites from ultramafic rocks, which is difficult as e.g. UMLs can show many carbonatite-like features themselves. Deciphering multistage alteration processes is crucial for understanding element mobilization in carbonate-poor and carbonate-rich crustal environments. Interaction between carbonatitic liquids and silicate rocks can generate a wide range of petrological phenomena, from fenitization (Elliott et al., 2018) over formation of glimmerites and pyroxenites (Anenburg and Walters, 2024) to ijolitization (Vasyukova and Williams-Jones, 2022), with the latter producing ultramafic rocks through interaction with a carbonitic melt. However, this study serves as an example of how interaction between carbonatitic liquids and existing ultramafic rocks can develop, which is currently lacking in published literature.

CRediT authorship contribution statement

Felix Reinhard: Writing – review & editing, Writing – original draft, Visualization, Validation, Software, Methodology, Investigation, Formal analysis, Data curation, Conceptualization. **Benjamin F. Walter:** Writing – review & editing, Supervision, Resources, Funding acquisition, Conceptualization. **R. Johannes Giebel:** Writing – review & editing, Supervision, Software, Methodology, Data curation. **Armin Zeh:** Writing – review & editing, Visualization, Software, Resources, Data curation. **Michael A.W. Marks:** Writing – review & editing, Supervision, Resources, Conceptualization. **Gregor Markl:** Writing – review & editing, Supervision, Resources, Project administration, Methodology, Conceptualization.

Declaration of competing interest

The authors declare the following financial interests/personal relationships which may be considered as potential competing interests:

Benjamin Walter reports financial support was provided by German Research Foundation. If there are other authors, they declare that they have no known competing financial interests or personal relationships that could have appeared to influence the work reported in this paper.

Acknowledgements

This study was funded by the German Science Foundation [DFG grant WA 3116/4–1] to Benjamin Walter. We thank the Ministry for Mines and Energy, Namibia, for their support and Pete Siegfried (Geo-Africa Prospecting) for logistical assistance during fieldwork. Special thanks to Sebastian Tappe for valuable input on nomenclature, Jorge

Arthuzzi and Annalena Salvi for proofreading. We also appreciate Christoph Glotzbach for his hands-on instruction in (U-Th-Sm)/He dating, which enriched this work. Further thanks go to Elisabeth Eiche, Claudia Mössner and Maya Denker for support with whole-rock analyses. Finally, we acknowledge Michael Anenburg and the anonymous reviewer for constructive reviews and thank Gregory Shellnutt for editorial guidance.

Appendix A. Supplementary data

Supplementary data to this article can be found online at https://doi.org/10.1016/j.lithos.2025.108317.

References

Abersteiner, A., Kamenetsky, V.S., Pearson, D.G., Kamenetsky, M., Goemann, K., Ehrig, K., Rodemann, T., 2018. Monticellite in group-I kimberlites: Implications for evolution of parental melts and post-emplacement CO2 degassing. Chemical Geology 478, 76–88. https://doi.org/10.1016/j.chemgeo.2017.06.037.

Anenburg, M., Mavrogenes, J.A., 2018. Carbonatitic versus hydrothermal origin for fluorapatite REE-Th deposits: experimental study of REE transport and crustal "antiskarn" metasomatism. Am. J. Sci. 318 (3), 335–366. https://doi.org/10.2475/03.2018.03.

Anenburg, M., Walters, J.B., 2024. Metasomatic ijolite, glimmerite, silicocarbonatite, and antiskarn formation: carbonatite and silicate phase equilibria in the system $Na2O–CaO–K_2O–FeO–MgO–Al_2O_3–SiO_2–H_2O–O_2–CO_2$. Contrib. Mineral. Petrol. 179 (5), 40. https://doi.org/10.1007/s00410-024-02109-0.

Armstrong, J.T., 1991. In: Heinrich, K.F.J., Newbury, D.E. (Eds.), Quantitative elemental analysis of individual microparticles with electron beam instruments. Electron Probe Quantitation, pp. 261–315. https://doi.org/10.1007/978-1-4899-2617-3_15.

Bial, J., Büttner, S.H., Frei, D., 2015. Formation and emplacement of two contrasting late-Mesoproterozoic magma types in the central Namaqua Metamorphic complex (South Africa, Namibia): evidence from geochemistry and geochronology. Lithos 224–225, 272–294. https://doi.org/10.1016/j.lithos.2015.02.021.

Blanco, G., Germs, G.J.B., Rajesh, H.M., Chemale, F., Dussin, I.A., Justino, D., 2011. Provenance and paleogeography of the Nama Group (Ediacaran to early Palaeozoic, Namibia): petrography, geochemistry and U–Pb detrital zircon geochronology. Precambrian Res. 187 (1–2), 15–32. https://doi.org/10.1016/j.precamres.2011.02.002.

Braunger, S., Marks, M.A.W., Walter, B.F., Neubauer, R., Reich, R., Wenzel, T., Parsapoor, A., Markl, G., 2018. The petrology of the Kaiserstuhl Volcanic complex, SW Germany: the importance of metasomatized and oxidized lithospheric mantle for carbonatite generation. J. Petrol. 59 (9), 1731–1762. https://doi.org/10.1093/petrology/egy078.

Brod, J.A., Gaspar, J.C., De Araújo, D.P., Gibson, S.A., Thompson, R.N., Junqueira-Brod, T.C., 2001. Phlogopite and tetra-ferriphlogopite from Brazilian carbonatite complexes: Petrogenetic constraints and implications for mineral-chemistry systematics. J. Asian Earth Sci. 19 (3), 265–296. https://doi.org/10.1016/S1367-9120(00)00047-X.

Cesare, B., Nestola, F., Johnson, T., Mugnaioli, E., Della Ventura, G., Peruzzo, L., Bartoli, O., Viti, C., Erickson, T., 2019. Garnet, the archetypal cubic mineral, grows tetragonal. Sci. Rep. 9 (1), 14672. https://doi.org/10.1038/s41598-019-51214-9.

Chmyz, L., Azzone, R.G., Ruberti, E., Marks, M.A., dos Santos, T.J.S., 2022. Olivines as probes into assimilation of silicate rocks by carbonatite magmas: Unraveling the genesis of reaction rocks from the Jacupiranga alkaline-carbonatite complex, southern Brazil. Lithos 416, 106647. https://doi.org/10.1016/j.lithos.2022.106647.

Chmyz, L., Azzone, R.G., Ruberti, E., Guarino, V., 2025. Wall rock assimilation in carbonatite magmas: Textural, mineral and whole-rock geochemical signatures in the Jacupiranga complex, Brazil. Geochemistry 85 (1), 126218. https://doi.org/10.1016/j.chemer.2024.126218.

Davies, G.R., Spriggs, A.J., Nixon, P.H., 2001. A non-cognate origin for the gibeon kimberlite megacryst suite, Namibia: implications for the origin of Namibian Kimberlites. J. Petrol. 42 (1), 159–172. https://doi.org/10.1093/petrology/42.1.159.

Diener, J.F.A., Thomas, R.J., Macey, P.H., 2017. Pan-African accretionary metamorphism in the Sperrgebiet Domain, Gariep Belt, SW Namibia. Precambrian Res. 292, 152–162. https://doi.org/10.1016/j.precamres.2017.02.006.

Doroshkevich, A., Prokopyev, I., Kruk, M., Sharygin, V., Izbrodin, I., Starikova, A., Ponomarchuk, A., Izokh, A., Nugumanova, Y., 2022. Age and petrogenesis of ultramafic lamprophyres of the Arbarastakh alkaline-carbonatite complex, Aldan-Stanovoy shield, South of Siberian Craton (Russia): Evidence for ultramafic lamprophyre-carbonatite link. Journal of Petrology 63 (9), egac073. https://doi.org/10.1093/petrology/egac073.

Dristas, J.A., Martínez, J.C., Massonne, H.-J., Pimentel, M.M., 2013. Mineralogical and geochemical characterization of a rare ultramafic lamprophyre in the Tandilia belt basement, Río de la Plata Craton, Argentina. J. S. Am. Earth Sci. 43, 46–61. https://doi.org/10.1016/j.jsames.2013.01.002.

Ehlers, T.A., Farley, K.A., 2003. Apatite (U–Th)/he thermochronometry: methods and applications to problems in tectonic and surface processes. Earth Planet. Sci. Lett. 206 (1–2), 1–14. https://doi.org/10.1016/S0012-821X(02)01069-5.

Elliott, H.A.L., Wall, F., Chakhmouradian, A.R., Siegfried, P.R., Dahlgren, S., Weatherley, S., Finch, A.A., Marks, M.A.W., Dowman, E., Deady, E., 2018. Fenites associated with carbonatite complexes: a review. Ore Geol. Rev. 93, 38–59. https://doi.org/10.1016/j.oregeorev.2017.12.003.

Farley, K.A., 2002. (U-Th)/he dating: Techniques, calibrations, and applications. Rev. Mineral. Geochem. 47 (1), 819–844. https://doi.org/10.2138/rmg.2002.47.18.

Fraser, K.J., Hawkesworth, C.J., Erlank, A.J., Mitchell, R.H., Scott-Smith, B.H., 1985. Sr, Nd and Pb isotope and minor element geochemistry of lamproites and kimberlites. Earth Planet. Sci. Lett. 76 (1–2), 57–70. https://doi.org/10.1016/0012-821X(85)90148-7.

Gerdes, A., Zeh, A., 2006. Combined U–Pb and Hf isotope LA-(MC-)ICP-MS analyses of detrital zircons: Comparison with SHRIMP and new constraints for the provenance and age of an Armorican metasediment in Central Germany. Earth Planet. Sci. Lett. 249 (1–2), 47–61. https://doi.org/10.1016/j.epsl.2006.06.039.

Gerdes, A., Zeh, A., 2009. Zircon formation versus zircon alteration—New insights from combined U–Pb and Lu–Hf in-situ LA-ICP-MS analyses, and consequences for the interpretation of Archean zircon from the Central Zone of the Limpopo Belt. Chem. Geol. 261 (3–4), 230–243. https://doi.org/10.1016/j.chemgeo.2008.03.005.

Germs, G.J.B., Knoll, A.H., Vidal, G., 1986. Latest proterozoic microfossils from the nama group, Namibia (south West Africa). Precambrian Res. 32 (1), 45–62. https://doi.org/10.1016/0301-9268(86)90029-X.

Giebel, R.J., Marks, M.A.W., Gauert, C.D.K., Markl, G., 2019. A model for the formation of carbonatite-phoscorite assemblages based on the compositional variations of mica and apatite from the Palabora Carbonatite complex, South Africa. Lithos 324–325, 89–104. https://doi.org/10.1016/j.lithos.2018.10.030.

Giuliani, A., 2018. Insights into kimberlite petrogenesis and mantle metasomatism from a review of the compositional zoning of olivine in kimberlites worldwide. Lithos 312–313, 322–342. https://doi.org/10.1016/j.lithos.2018.04.029.

Giuliani, A., Soltys, A., Phillips, D., Kamenetsky, V.S., Maas, R., Goemann, K., Woodhead, J.D., Drysdale, R.N., Griffin, W.L., 2017. The final stages of kimberlite petrogenesis: Petrography, mineral chemistry, melt inclusions and Sr-C-O isotope geochemistry of the Bultfontein kimberlite (Kimberley, South Africa). Chem. Geol. 455, 342–356. https://doi.org/10.1016/j.chemgeo.2016.10.011.

Glotzbach, C., Reinecker, J., Danišík, M., Rahn, M., Frisch, W., Spiegel, C., 2010. Thermal history of the central Gotthard and Aar massifs, European Alps: evidence for steady state, long-term exhumation. J. Geophys. Res. Earth 115 (F3). https://doi.org/10.1029/2009JF001304.

Gudfinnsson, G.H., Presnall, D.C., 2005. Continuous gradations among primary carbonatitic, kimberlitic, melilititic, basaltic, picritic, and komatiitic melts in equilibrium with garnet lherzolite at 3–8 GPa. Journal of Petrology 46 (8), 1645–1659. https://doi.org/10.1093/petrology/egi029.

Howarth, G.H., Moore, A.E., Harris, C., van der Meer, Q.H., le Roux, P., 2019. Crustal versus mantle origin of carbonate xenoliths from Kimberley region kimberlites using CO-Sr-Nd-Pb isotopes and trace element abundances. Geochim. Cosmochim. Acta 266, 258–273. https://doi.org/10.1016/j.gca.2019.03.026.

Janse, A., 1971. Monticellite bearing porphyritic peridotite from Gross Brukkaros, South West Africa. Verhandel. Die Geol. Verenig. Suid Afrika = Transact. Geol. Soc. S. Afr. 74 (2), 45–55.

Kasay, G.M., Borst, A.M., Giebel, J.R., Bolarinwa, A.T., Beranoaguirre, A., Kluge, T., Aromolaran, O.K., Raza, M., Eiche, E., Kolb, J., Nzolang, C., Walter, B.F., 2024. Petrogenesis and geodynamic setting of the Bingo alkaline-carbonatite complex, DRC: Constraints from petrography, geochemistry, C-O isotopes and U-Pb geochronology. Precambrian Res. 408, 107421. https://doi.org/10.1016/j.precamres.2024.107421.

Krüger, J.C., Romer, R.L., Kämpf, H., 2013. Late Cretaceous ultramafic lamprophyres and carbonatites from the Delitzsch Complex, Germany. Chemical Geology 353, 140–150. https://doi.org/10.1016/j.chemgeo.2012.09.026.

Kurszlaukis, S., 1994. Geology and Geochemistry of the Carbonatitic Gross Brukkaros Volcanic Field and the Ultrabasic Blue Hills Intrusive Complex, southern Namibia [Dissertation].. University of Würzburg.

Kurszlaukis, S., Franz, L., Brey, G.P., 1999. The Blue Hills Intrusive complex in Southern Namibia—Relationships between carbonatites and monticellite picrites. Chem. Geol. 160 (1–2), 1–18. https://doi.org/10.1016/S0009-2541(99)00027-3.

Le Bas, M.J., 2008. Fenites associated with Carbonatites. Can. Mineral. 46 (4), 915–932. https://doi.org/10.3749/canmin.46.4.915.

Le Maitre, R.W., Streckeisen, A., Zanettin, B., Le Bas, M.J., Bonin, B., Bateman, P., Bellieni, G., Dudek, A., Efremova, S., Keller, J., Lameyre, J., Sabine, P.A., Schmid, R., Sorensen, H., Woolley, A.R., 2002. Igneous Rocks - A Classification and Glossary of Terms: Recommendations of the International Union of Geological Sciences Subcommission on the Systematics of Igneous Rocks, 2. Edition, Cambridge.

Li, W.Y., Yu, H.M., Xu, J., Halama, R., Bell, K., Nan, X.Y., Huang, F., 2020. Barium isotopic composition of the mantle: Constraints from carbonatites. Geochim. Cosmochim. Acta 278, 235–243. https://doi.org/10.1016/j.gca.2019.06.041.

Lodders, K., Fegley, B., 1998. The Planetary Science Companion. Oxford Univ. Press.

Lorenz, V., Kurszlaukis, S., 1997. Volcanological features of a low-viscosity melt: the carbonatitic Gross Brukkaros Volcanic Field, Namibia. Bull. Volcanol. 58 (6), 421–431. https://doi.org/10.1007/s004450050150.

Lorenz, V., Stachel, T., Kurszlaukis, S., Stanistreet, I.G., 2000. Volcanology of the Gross Brukkaros Field, southern Namibia. Commun. Geol. Surv. Namibia 12, 395–401.

Mitchell, R.H., 1986. Mineralogy of Kimberlites. In: Kimberlites. Springer, Boston, MA. https://doi.org/10.1007/978-1-4899-0568-0_6.

Mitchell, R.H., 1995. Kimberlites and orangeites. Kimberl. Orang. Rel. Rocks 1-90. https://doi.org/10.1007/978-1-4615-1993-5_1.

Mitchell, R.H., Giuliani, A., O'Brien, H., 2019. What is a Kimberlite? Petrology and Mineralogy of Hypabyssal Kimberlites. Elements 15 (6), 381–386. https://doi.org/10.2138/gselements.15.6.381.

Muramatsu, Y., Wedepohl, K.H., 1985. REE and selected trace elements in kimberlites from the Kimberley area (South Africa). Chem. Geol. 51 (3–4), 289–301. https://doi.org/10.1016/0009-2541(85)90138-X.

Nielsen, T.F.D., Sand, K.K., 2008. The Majuagaa Kimberlite dike, Maniitsoq region, West Greenland: Constraints on an Mg-rich silicocarbonatitic melt composition from groundmass mineralogy and bulk compositions. Can. Mineral. 46 (4), 1043–1061. https://doi.org/10.3749/canmin.46.4.1043.

Noble, R.H., Macintyre, R.M., Brown, P.E., 1988. Age constraints on Atlantic evolution: timing of magmatic activity along the E Greenland continental margin. Geol. Soc. Lond. Spec. Publ. 39 (1), 201–214. https://doi.org/10.1144/GSL.SP.1988.039.01.19.

Pandey, R., Rao, N.V.C., Dhote, P., Pandit, D., Choudhary, A.K., Sahoo, S., Lehmann, B., 2018. Rift-associated ultramafic lamprophyre (damtjernite) from the middle part of the lower cretaceous (125 Ma) succession of Kutch, northwestern India: Tectonomagmatic implications. Geosci. Front. 9 (6), 1883–1902. https://doi.org/10.1016/j.gsf.2017.10.013.

Paton, C., Woodhead, J.D., Hellstrom, J.C., Hergt, J.M., Greig, A., Maas, R., 2010. Improved laser ablation U-Pb zircon geochronology through robust downhole fractionation correction. Geochem. Geophys. Geosyst. 11 (3). https://doi.org/10.1029/2009GC002618.

Prokopyev, I., Starikova, A., Doroshkevich, A., Nugumanova, Y., Potapov, V., 2020. Petrogenesis of ultramafic lamprophyres from the Terina complex (Chadobets upland, Russia): Mineralogy and melt inclusion composition. Minerals 10 (5), 419. https://doi.org/10.3390/min10050419.

Reguir, E.P., Chakhmouradian, A.R., Halden, N.M., Malkovets, V.G., Yang, P., 2009. Major- and trace-element compositional variation of phlogopite from kimberlites and carbonatites as a petrogenetic indicator. Lithos 112, 372–384. https://doi.org/10.1016/j.lithos.2009.05.023.

Reguir, E.P., Camacho, A., Yang, P., Chakhmouradian, A.R., Kamenetsky, V.S., Halden, N.M., 2010. Trace-element study and uranium-lead dating of perovskite from the Afrikanda plutonic complex, Kola Peninsula (Russia) using LA-ICP-MS. Mineral. Petrol. 100 (3–4), 95–103. https://doi.org/10.1007/s00710-010-0131-9.

Rock, N.M.S., 1986. The Nature and Origin of Ultramafic Lamprophyres: Alnöites and Allied Rocks. J. Petrol. 27 (1), 155–196. https://doi.org/10.1093/petrology/27.1.155.

Rock, N.M.S., 1991. Nature, origin and evolution of lamprophyre melts. Lamprophyres 125–149. https://doi.org/10.1007/978-1-4757-0929-2_8.

Russell, J.K., Porritt, L.A., Lavallée, Y., Dingwell, D.B., 2012. Kimberlite ascent by assimilation-fuelled buoyancy. Nature 481 (7381), 352–356. https://doi.org/10.1038/nature10740.

Smith, B.H.S., Skinner, E.M., Clement, C.R., 1983. Further data on the occurrence of pectolite in kimberlite. Mineral. Mag. 47 (342), 75–78. https://doi.org/10.1180/minmag.1983.047.342.13.

Secher, K., Heaman, L.M., Nielsen, T.F.D., Jensen, S.M., Schjøth, F., Creaser, R.A., 2009. Timing of kimberlite, carbonatite, and ultramafic lamprophyre emplacement in the alkaline province located 64–67 N in southern West Greenland. Lithos 112, 400–406. https://doi.org/10.1016/j.lithos.2009.04.035.

Smith, B.H.S., Nowicki, T.E., Russell, J.K., Webb, K.J., Mitchell, R.H., Hetman, C.M., Robey, J.V., 2018. A Glossary of Kimberlite and Related Terms. Scott-Smith Petrology Inc.

Soltys, A., Giuliani, A., Phillips, D., 2018. Crystallisation sequence and magma evolution of the De Beers dyke (Kimberley, South Africa). Mineral. Petrol. 112 (2), 503–518. https://doi.org/10.1007/s00710-018-0588-5.

Sparks, R.S.J., Brooker, R.A., Field, M., Kavanagh, J., Schumacher, J.C., Walter, M.J., White, J., 2009. The nature of erupting kimberlite melts. Lithos 112, 429–438. https://doi.org/10.1016/j.lithos.2009.05.032.

Spriggs, A.J., 1988. An Isotopic and Geochemical Study of Kimberlites and Associated Alkaline Rocks from Namibia [Dissertation]. University of Leeds.

Stacey, J.S., Kramers, J.D., 1975. Approximation of terrestrial lead isotope evolution by a two-stage model. Earth Planet. Sci. Lett. 26 (2), 207–221. https://doi.org/10.1016/0012-821X(75)90088-6.

Stachel, T., Lorenz, V., Stanistreet, I.G., 1994. Gross Brukkaros (Namibia) - an enigmatic crater-fill reinterpreted as due to cretaceous caldera evolution. Bull. Volcanol. 56 (5), 386–397. https://doi.org/10.1007/BF00326464.

Stanistreet, I.G., Kukla, P.A., Henry, G., 1991. Sedimentary basinal responses to a late Precambrian Wilson Cycle: the Damara Orogen and Nama Foreland, Namibia. J. Afr. Earth Sci. (Middle East) 13 (1), 141–156. https://doi.org/10.1016/0899-5362(91)90048-4.

Su, K., Zhang, S.B., Li, Z.X., Zhang, L., Liang, T., Du, Y., Li, L., 2023. When carbonatite met granite: a carbonatite magma-wall rock reaction origin for the Paleoproterozoic pyroxenite and syenite in Fengzhen, North China. Lithos 454, 107231. https://doi.org/10.1016/j.lithos.2023.107231.

Sudholz, Z.J., Reddicliffe, T.H., Jaques, A.L., Yaxley, G.M., Haynes, M., Gorbatov, A., Czarnota, K., Frigo, C., Maas, R., Knowles, B., 2023. Petrology, age, and rift origin of ultramafic lamprophyres (aillikites) at Mount Webb, a new alkaline province in Central Australia. Geochemistry, Geophysics, Geosystems 24 (10). https://doi.org/10.1029/2023GC011120 e2023GC011120.

Sun, S.S., McDonough, W.F., 1989. Chemical and isotopic systematics of oceanic basalts: Implications for mantle composition and processes. Geol. Soc. Lond. Spec. Publ. 42 (1), 313–345. https://doi.org/10.1144/GSL.SP.1989.042.01.19.

Tappe, S., Jenner, G.A., Foley, S.F., Heaman, L., Besserer, D., Kjarsgaard, B.A., Ryan, B., 2004. Torngat ultramafic lamprophyres and their relation to the North Atlantic Alkaline Province. Lithos 76 (1–4), 491–518. https://doi.org/10.1016/j.lithos.2004.03.040.

Tappe, S., Foley, S.F., Jenner, G.A., Kjarsgaard, B.A., 2005. Integrating Ultramafic Lamprophyres into the IUGS Classification of Igneous Rocks: Rationale and Implications. J. Petrol. 46 (9), 1893–1900. https://doi.org/10.1093/petrology/egi039.

Tappe, S., Foley, S.F., Jenner, G.A., Heaman, L.M., Kjarsgaard, B.A., Romer, R.L., Stracke, A., Joyce, N., Hoefs, J., 2006. Genesis of Ultramafic Lamprophyres and Carbonatites at Aillik Bay, Labrador: a consequence of Incipient Lithospheric Thinning beneath the North Atlantic Craton. J. Petrol. 47 (7), 1261–1315. https://doi.org/10.1093/petrology/egl008.

Tappe, S., Stracke, A., Van Acken, D., Strauss, H., Luguet, A., 2020. Origins of kimberlites and carbonatites during continental collision – Insights beyond decoupled Nd-Hf isotopes. Earth Sci. Rev. 208, 103287. https://doi.org/10.1016/j.earscirev.2020.103287.

Tera, F., Wasserburg, G.J., 1972. U-Th-Pb systematics in three Apollo 14 basalts and the problem of initial Pb in lunar rocks. Earth Planet. Sci. Lett. 14 (3), 281–304. https://doi.org/10.1016/0012-821X(72)90128-8.

Vasyukova, O.V., Williams-Jones, A.E., 2022. Carbonatite metasomatism, the key to unlocking the carbonatite-phoscorite-ultramafic rock paradox. Chem. Geol. 602, 120888. https://doi.org/10.1016/j.chemgeo.2022.120888.

Veter, M., Foley, S.F., Mertz-Kraus, R., Groschopf, N., 2017. Trace elements in olivine of ultramafic lamprophyres controlled by phlogopite-rich mineral assemblages in the mantle source. Lithos 292–293, 81–95. https://doi.org/10.1016/j.lithos.2017.08.020.

Von Knorring, O., 1962. Geochemical characteristics of carbonatites. Nature 194 (4831), 860–861. https://doi.org/10.1038/194860b0.

Walter, B.F., Giebel, R.J., Steele-MacInnis, M., Marks, M.A.W., Kolb, J., Markl, G., 2021. Fluids associated with carbonatitic magmatism: a critical review and implications for carbonatite magma ascent. Earth Sci. Rev. 215, 103509. https://doi.org/10.1016/j.earscirev.2021.103509.

Walter, B.F., Giebel, R.J., Siegfried, P.R., Gudelius, D., Kolb, J., 2023. The eruption interface between carbonatitic dykes and diatremes – the Gross Brukkaros volcanic field Namibia. Chem. Geol. 621, 121344. https://doi.org/10.1016/j.chemgeo.2023.121344.

Yaxley, G.M., Anenburg, M., Tappe, S., Decree, S., Guzmics, T., 2022. Carbonatites: Classification, sources, Evolution, and Emplacement. Annu. Rev. Earth Planet. Sci. 50 (1), 261–293. https://doi.org/10.1146/annurev-earth-032320-104243.

Zindler, A., Hart, S., 1986. Chemical Geodynamics, 14. Annual Reviews, Inc., pp. 493–571